J. Fluid Mech. (2005), *vol.* 528, *pp.* 323–354. © 2005 Cambridge University Press
doi:10.1017/S002211200500340X Printed in the United Kingdom

The role of tertiary wave interactions in wave–body problems

By B. MOLIN[1], F. REMY[1], O. KIMMOUN[1] AND E. JAMOIS[1,2]

[1]École Supérieure d'Ingénieurs de Marseille, 13 451 Marseille cedex 20, France

[2]Saipem SA, 78 884 Saint-Quentin Yvelines cedex, France

(Received 16 June 2004 and in revised form 8 November 2004)

Results from experiments on wave interaction with a rigid plate are reported. The plate is projected from one of the sidewalls of the basin. The sidewall acts as a plane of symmetry, thereby doubling the widths of the plate and of the basin. The tests are carried out in regular waves of varying periods and steepnesses. At wavelengths comparable with the width of the plate, strong run-ups are observed at the plate–wall intersection, increasing with the wave steepness. These run-ups take many wave cycles to develop, with no steady state being reached in some cases. It is advocated that these phenomena result from third-order interactions between the incident and reflected wave fields, over a wide area on the weather side of the plate. A theoretical model is proposed, based on tertiary wave interaction. A parabolic equation is derived that describes the transformation of the incoming waves through their interaction with the reflected wave field. A steady-state solution is obtained through iterations. Results from the theoretical model are compared with the experimental data, with good agreement.

1. Introduction

Wave loads upon large bodies are nowadays routinely computed with so-called diffraction-radiation codes, which have reached an industrial stage. Being based upon linearized potential flow theory, these codes only yield the fundamental components of the wave loads and wave response, in the form of Response Amplitude Operators (RAOs). It is usually found from model tests or measurements at sea that the RAOs (as derived through spectral analysis of the records) are not sensitive to wave steepness. Nonlinear effects most often take the form of sub- and super-harmonic components (in the wave frequencies), the most widely known and studied being the slow-drift and springing forces which are of second-order in the wave steepness (e.g. see Molin 1994).

A particular situation where the RAOs seem to vary with wave steepness is the case of a ship or barge in beam seas, at zero forward speed. Large free-surface elevations, known as 'run-up', can sometimes be seen at midship, in complete disagreement with the predictions of linearized potential flow codes. These run-up effects depend very much upon the steepness of the incoming waves.

An example is provided by the time traces shown in figure 1. They relate to a large rectangular barge model (length 5 m, width 1.2 m, draft 0.24 m) tested in the experimental facilities of Cehipar (el Pardo, Spain). The irregular sea-state (of Pierson–Moskowitz type) produced has a significant wave height of 0.15 m and a peak

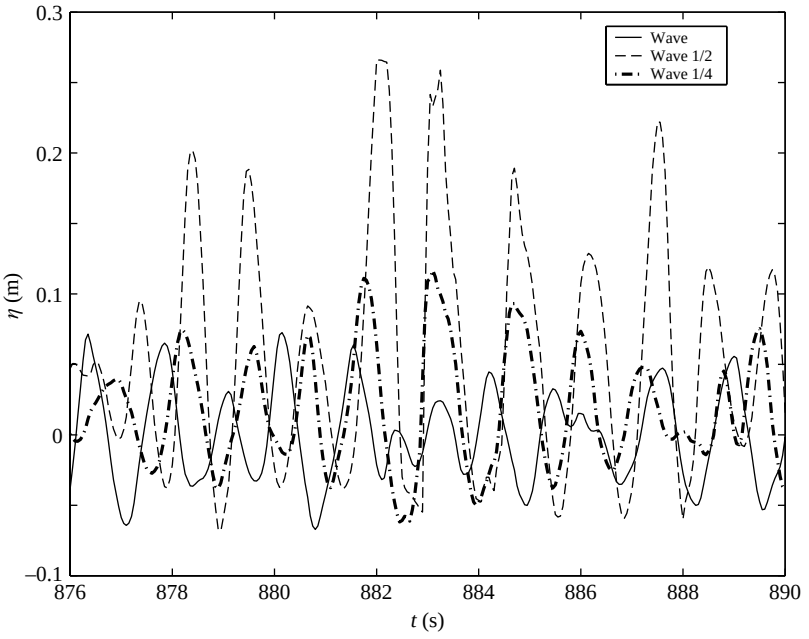

FIGURE 1. Model tests on a barge model in irregular beam seas. Time series of the relative free-surface elevation at midship ('Wave 1/2'), at one quarter length ('Wave 1/4') and away from the barge model ('Wave'). $H_S = 0.15$ m, $T_p = 1.6$ s, $\gamma = 1$.

period of 1.6 s, meaning a steepness $H_S/L_P = H_S/(1.56\,T_P^2)$ less than 4 %. Figure 1 shows time series of the free-surface elevation away from the barge, that is the incoming waves (with some contamination from the radiated and diffracted wave systems), and of the relative free-surface elevations as measured with two gauges attached to the barge hull, on the weather side. The first gauge is located at midship ('Wave 1/2' in the figure), the second one at mid-distance from midship to the bow ('Wave 1/4'). It can be seen that the crest to trough values of the relative elevations at midship are about twice the values at a quarter length. Linear calculations (not shown) give quasi-identical RAO values at the two locations. What can also be seen in the figure, and will be made clear further on, is that the relative elevation at midship is lagging in time behind the quarter length one.

A view of the run-up effect, as photographed during another experimental campaign in the experimental facilities of BGO-First, at la Seyne sur mer, is provided in figure 2.

It is advocated in this paper that these phenomena result from tertiary ('third-order') interactions, between the incoming wave system and the reflected wave system from the structure, taking place over a wide area on its weather side. This statement is based upon thorough analysis of dedicated model tests and upon a theoretical model.

The experiments, described in § 2, consisted in submitting a vertical plate to regular waves of varying wavelengths and steepnesses. The instrumentation consisted of wave gauges along the plate and in between the plate and the wavemakers. A striking feature of these tests is the transient character of the time series of the free-surface elevations along the plate: their amplitudes vary slowly in time, at rates that depend on the square of the wave steepness. They also slowly lag in time behind the reference incoming waves, at rates that, again, depend on the square of the steepness. Large run-up effects are obtained over a wide range of wavelengths.

FIGURE 2. Run-up on a barge model at BGO-First.

The theoretical model is described in § 3. It is approximate in that the reflected wave system by the plate is locally idealized as a plane wave. Use is then made of existing theory on tertiary plane wave interaction (Longuet-Higgins & Phillips 1962) to derive the local modification of the complex amplitude of the incoming wave, which obeys a parabolic equation (similar to the parabolic approximation of the mild slope equation). An iterative scheme is proposed to update successively the incoming and diffracted wave fields.

Comparisons between experiments and calculations are rendered difficult by the fact that the theoretical problem is solved in the frequency domain, expressing a steady-state solution, whereas no steady state was reached in many experimental tests, because of the long transient character of the observed phenomena: the exploitable part of the records is limited by the multiple wave reflections in between the plate and the wavemakers. In the cases where comparisons are possible, a good agreement is obtained.

2. Experimental results

2.1. *Test set-up*

The tests took place in the BGO-First offshore wave tank, which has a width of 16 m and a length of about 30 m from the wavemakers to the beach. The false bottom was lowered to a depth of 3 m.

The model consisted of a rigid plate, attached to one of the sidewalls. The width of the plate was 1.2 m, its thickness 5 cm and its height 2 m, of which 1.5 m were immersed. By geometric symmetry, the set-up was therefore equivalent to a plate 2.4 m wide in the middle of a basin 32 m wide. The plate was located 19.3 m from the wavemakers.

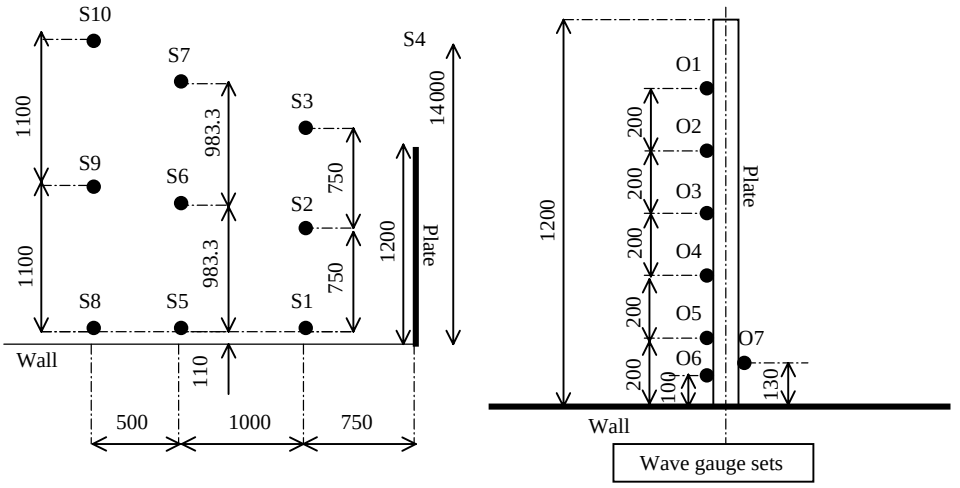

FIGURE 3. Experimental set-up.

The instrumentation consisted of wave gauges. Six capacitive gauges were set along the plate, on the weather side, at distances from the wall of 10 cm (gauge O6), 20 cm (O5), 40 cm (O4), 60 cm (O3), 80 cm (O2) and 1.0 m (O1). A seventh one (O7) was located on the lee side, 13 cm from the wall.

Nine resistive gauges were located in between the wavemakers and the plate, as shown in figure 3. A tenth one (S4) was located at the same x-coordinate as the capacitive gauges, away from the plate, 2 m from the opposite wall. It provided the more or less undisturbed incident-wave elevation.

The tests were performed in regular waves only, at wave periods of 0.88, 0.98, 1.07, 1.16, 1.24, 1.32 and 1.39 s. This means, for small-amplitude waves, wavelengths (L) of 1.2, 1.5, 1.8, 2.1, 2.4, 2.7 and 3.0 m. At each wave period, five different wave heights were produced, with steepnesses H/L equal to 2, 3, 4, 5 and 6 % (H being the crest-to-trough value). The waves were calibrated prior to installing the plate and the reflection coefficients from the beach were derived from wave measurements (with 5 gauges along the centreline). The reflection coefficients were always less than 8 %.

In spite of the limited size of the plate as compared to the width of the basin, the reflected wave field is strong and is re-reflected by the wavemakers, back to the plate. As a consequence, the exploitable duration of the measurements is reduced to twice the distance l, from the plate to the wavemakers, divided by the group velocity.

2.2. *Illustrative results*

We first consider the case of a period of 0.88 s (wavelength of 1.2 m) and a steepness H/L of 4 %. Figure 4 shows time traces of the free-surface elevations away from the plate (gauge S4) and along the plate (gauges O1 to O6). They are shown from the time the wavefront reaches the plate until re-reflected waves by the wavemakers start to interfere. This means about 65 cycles. All signals are normalized by the amplitude A_I of the incoming waves (so the top signal oscillates roughly between -1 and $+1$).

It can be observed that the amplitudes of all elevations measured along the plate slowly evolve in time, with no steady state being apparently reached, even after 60 cycles. At the two gauges by the outer end of the plate, the signals slowly decrease in time, whereas at the three gauges on the wall side, they slowly increase in time. By

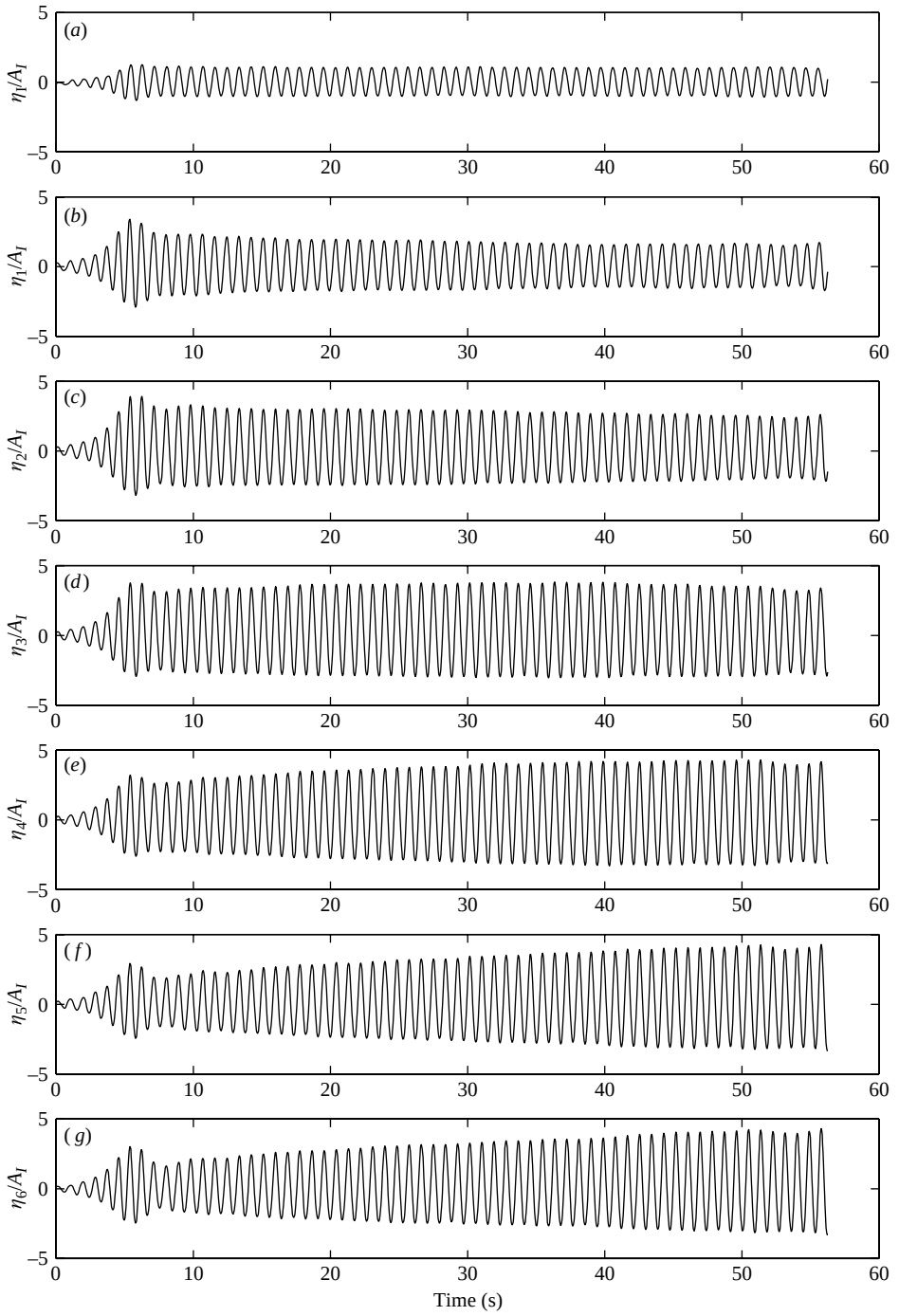

FIGURE 4. Wave period: 0.88 s; steepness H/L: 4 %. Time series of the normalized free-surface elevations (*a*) away from and (*b–g*) along the plate, from gauge O1 to gauge O6.

the end of the time traces, the amplitude of the free-surface motion by the plate–wall corner is about 4 times the amplitude of the incoming waves. Linear calculations give an RAO of about 1.75 (see figure 15).

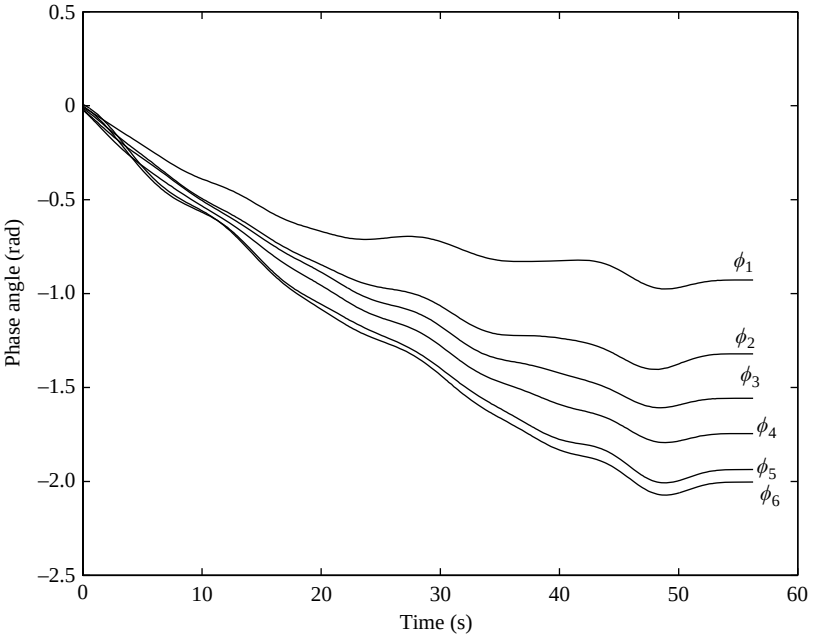

FIGURE 5. Associated phase lags.

Figure 5 complements figure 4 by showing the phase differences between the elevations measured along the plate and the incoming wave elevation away from the plate. They are obtained by Fourier analysis of the time series over sliding windows, three cycles long. It can be observed that the phase angles slowly decrease in time, with a value of -2 radians being reached at gauge O6 at the end of the record. This means that the free-surface elevation at the plate–wall corner is lagging behind that of the reference by about one-third of a wave period.

Next, still at the 0.88 s period, we consider the effect of varying the wave steepness. Figure 6 gives the time series of the free-surface elevation at gauge O6 (again normalized by the amplitude A_I of the incoming waves), for the five values of the steepness H/L. At the lowest value (2 %) a steady state is apparently quickly reached. At greater steepnesses again the amplitudes slowly increase in time, at rates that depend on the steepness: the greater the steepness the higher the rate of increase. At 5 % steepness, a steady state is apparently reached after about 20 cycles, with maximum elevations about 5 times the incoming-wave amplitude. At the greatest steepness (6 %), it looks as if no steady state is reached after the initial ramp that lasts for about 15 cycles. What actually happens is that the standing-wave pattern, in front of the plate, becomes so steep that the crests break.

Figure 7 complements figure 6 by showing the associated phase lags. Again they decrease in time, at rates that depend on the wave steepness, and seem to stabilize at -2.5 radians at the two greatest steepnesses.

Figure 8 shows the same phase lags with a stretched time scale, t being multiplied by the square of the steepness H/L. As a result, all the curves more or less coalesce together, at least during the initial phase. This shows that the rate of decrease of the phase lag is proportional to the square of the wave steepness.

Similarly, figure 9 shows the time evolution of the RAO of the free-surface elevation at gauge O6 (as obtained from the sliding window Fourier analysis) with the stretched

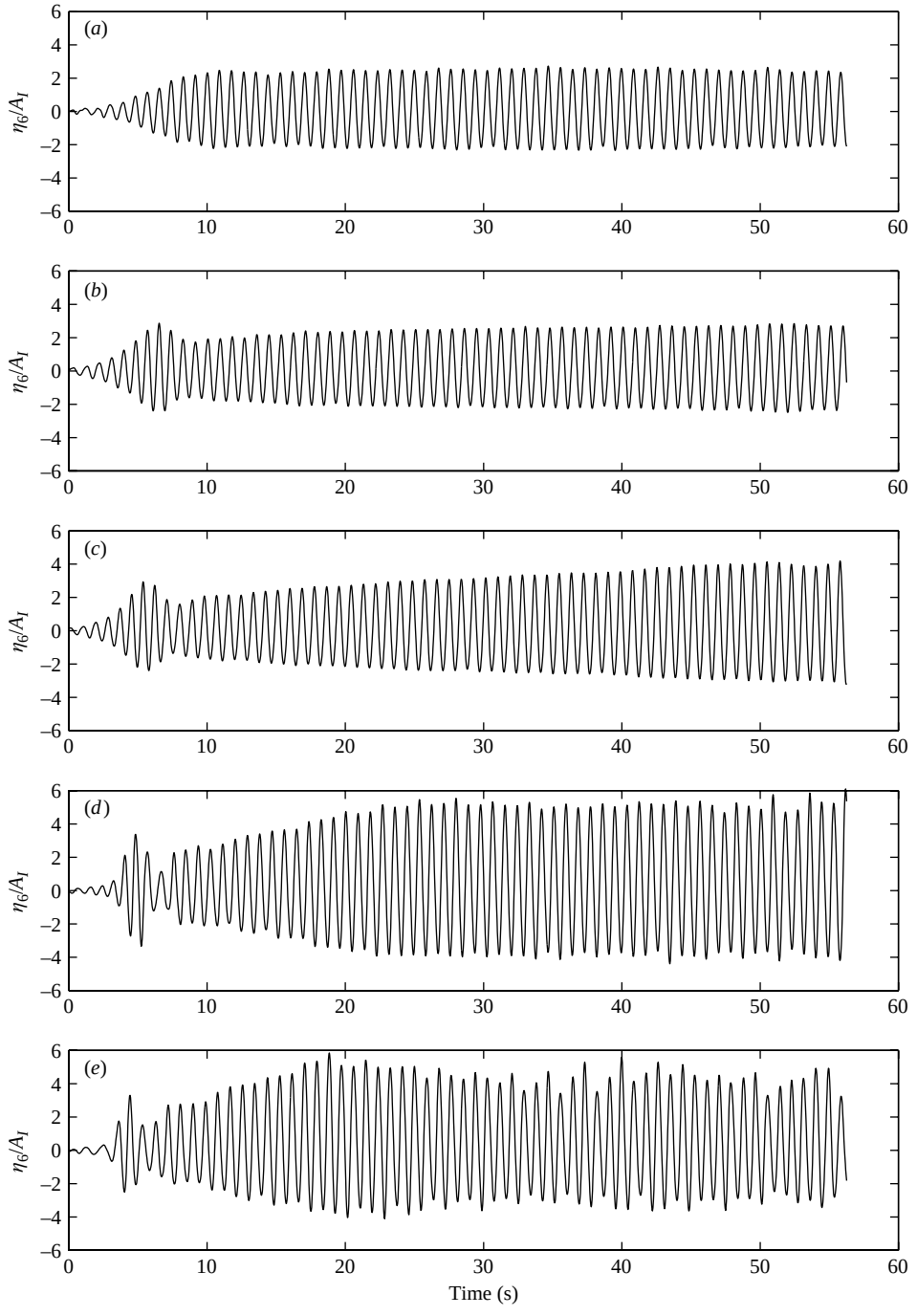

FIGURE 6. Time series of the normalized free-surface elevation at the plate–wall corner. Wave period: 0.88 s. Steepnesses (*a*) $H/L = 2\,\%$, (*b*) 3 %, (*c*) 4 %, (*d*) 5 %, (*e*) 6 %.

time scale $t \times (H/L)^2$. At the four greatest steepnesses, the slope of the initial part of the curves is the same, showing that the rate of increase of the RAO is also related to the square of the steepness.

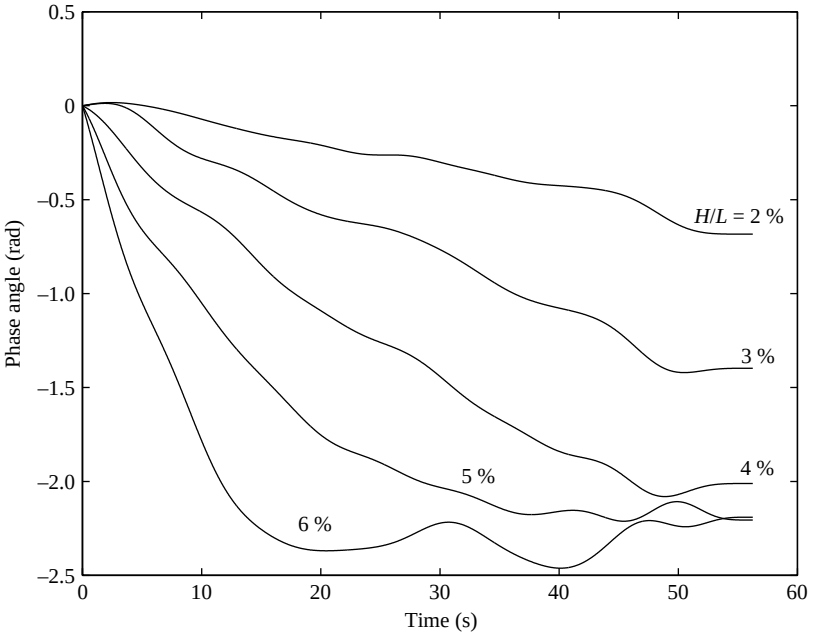

FIGURE 7. Phase lags at the plate–wall corner. $T = 0.88$ s. Steepnesses H/L from 2 to 6 %.

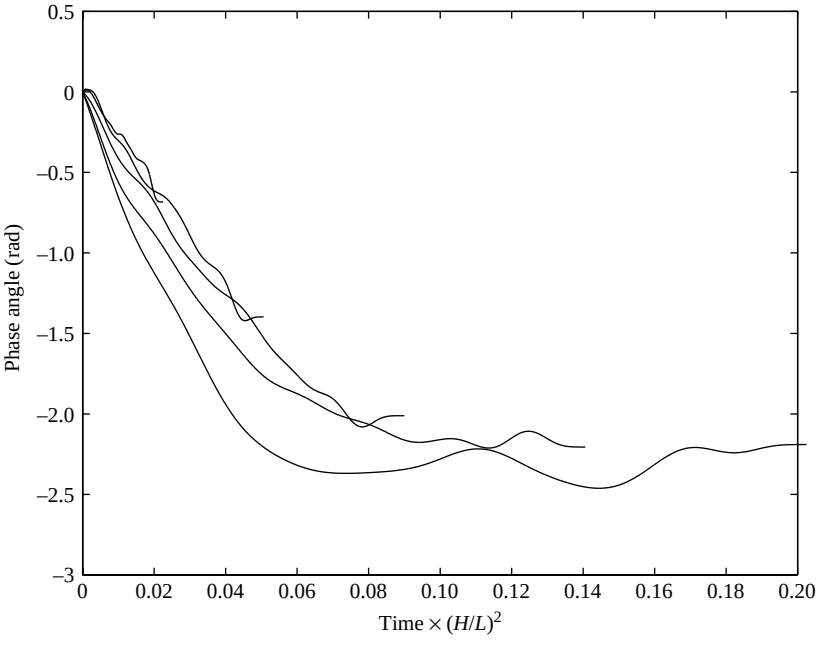

FIGURE 8. As figure 7 with stretched time scale.

These features are not limited to particular values of the wave period. They were observed at all periods with the most marked effects at 0.98 and 1.07 s. As an illustration, figures 10, 11 and 12 show similar results to figures 6, 8 and 9, for the 0.98 s wave period. At 6 % steepness, breaking is also observed, with a noticeable

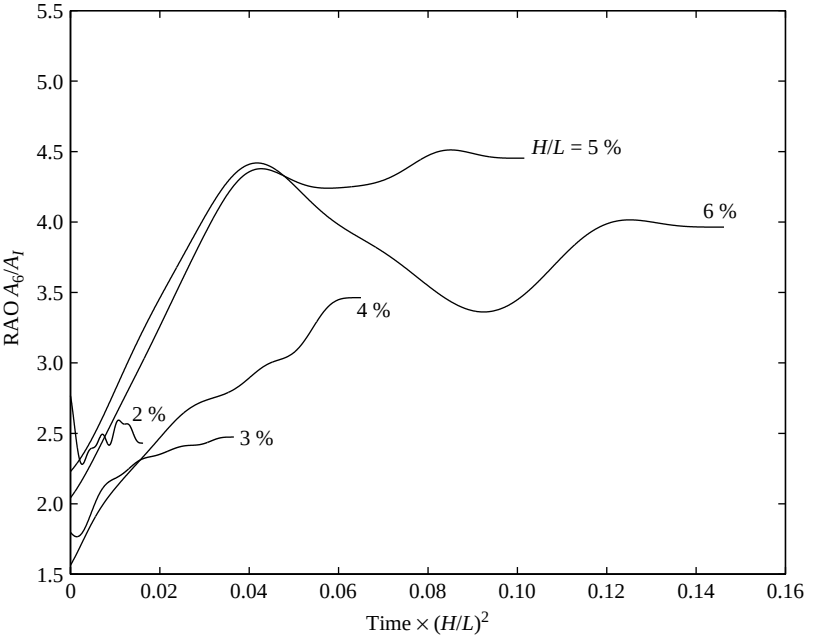

FIGURE 9. $T = 0.88$ s. Time evolution of the RAO at gauge O6 (stretched time scale).

period tripling effect (see figure 10*e*) as previously reported by Jiang, Perlin & Schultz (1998) and Longuet-Higgins & Drazen (2002).

2.3. *Interpretation*

An intuitive interpretation of the observed phenomena is that the reflected wave system acts as a shoal, slowing down the incoming waves which refract and diffract as they progress toward the plate. In the case of plane waves, it has been known for a long time (Longuet-Higgins & Phillips 1962) that tertiary interactions lead to mutual modifications of the phase velocities. The possible implications of this effect for wave–body problems have apparently never been considered. In the following section, we present a simple theoretical model where tertiary interactions are taken into account.

3. Theoretical model

3.1. *Tertiary interaction between plane waves*

For the sake of simplicity we restrict ourselves to two wave systems of identical frequencies, in infinite water-depth (which was the case for the tests). Longuet-Higgins & Phillips (1962) tackled the case of two different frequencies, in infinite water-depth (see also Tanaka 2002). Hogan, Gruman & Stiassnie (1988) considered the most general case of different frequencies in finite water-depth (also accounting for capillary effects).

We assume one wave component (with amplitude A_1) to propagate along the x-axis (the incoming waves) and the other one (with amplitude A_2) to propagate at an angle β. At first-order of approximation in the wave steepness, the free-surface elevation is written

$$\eta^{(1)} = A_1 \cos(k\,x - \omega\,t) + A_2 \cos(k\,x \cos\beta + k\,y \sin\beta - \omega\,t), \tag{3.1}$$

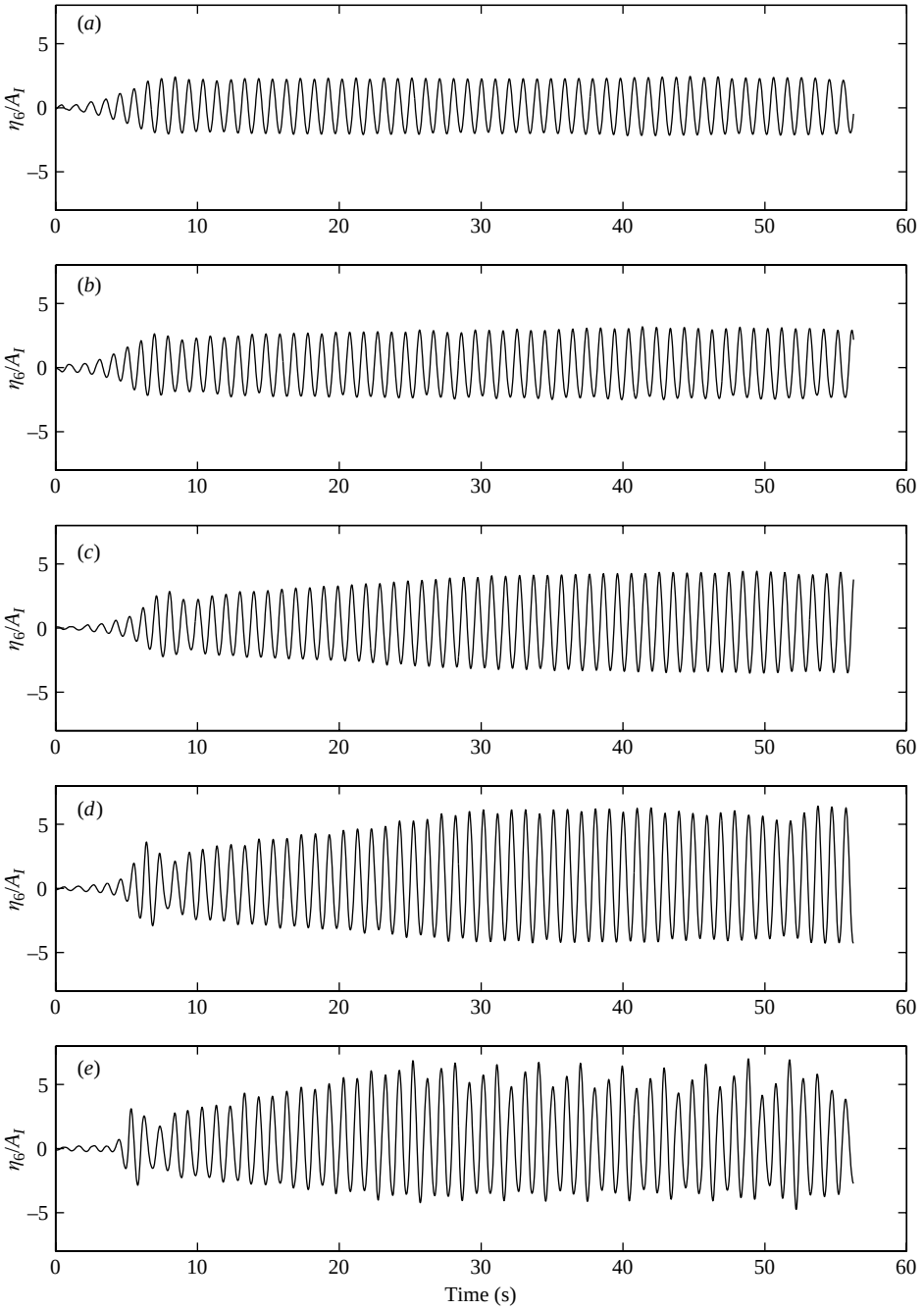

FIGURE 10. Time series of the normalized free-surface elevation at the plate–wall corner. Wave period: 0.98 s. Steepnesses (*a*) $H/L = 2\,\%$, (*b*) $3\,\%$, (*c*) $4\,\%$, (*d*) $5\,\%$, (*e*) $6\,\%$.

while the (linearized) velocity potential is

$$\Phi^{(1)} = \frac{A_1\, g}{\omega}\, \mathrm{e}^{k\,z}\, \sin(k\,x - \omega\,t) + \frac{A_2\, g}{\omega}\, \mathrm{e}^{k\,z}\, \sin(k\,x\, \cos\beta + k\,y\, \sin\beta - \omega\,t), \qquad (3.2)$$

the wavenumber k and the frequency ω being linked by the deep-water dispersion equation $\omega^2 = g\,k$.

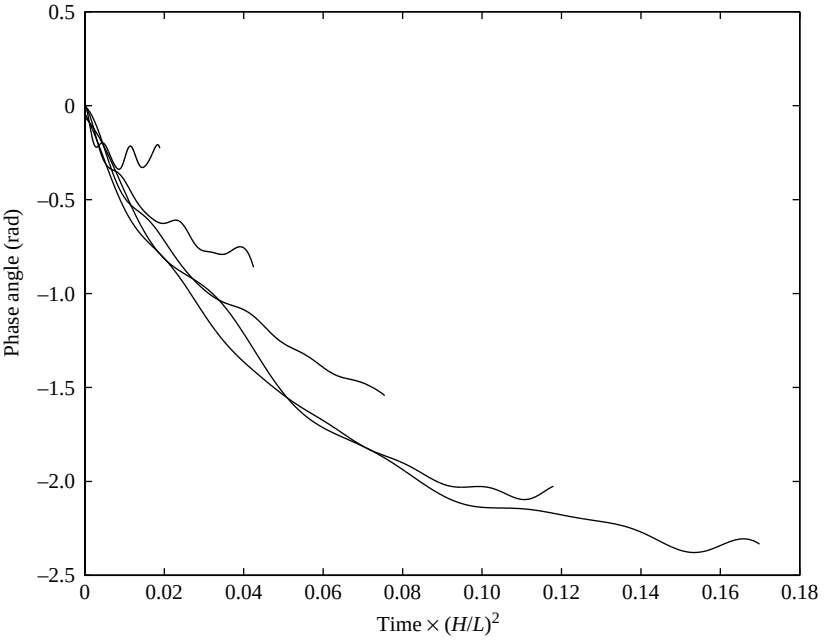

FIGURE 11. Time evolution of the phase lag (stretched time scale). Wave period: 0.98 s.

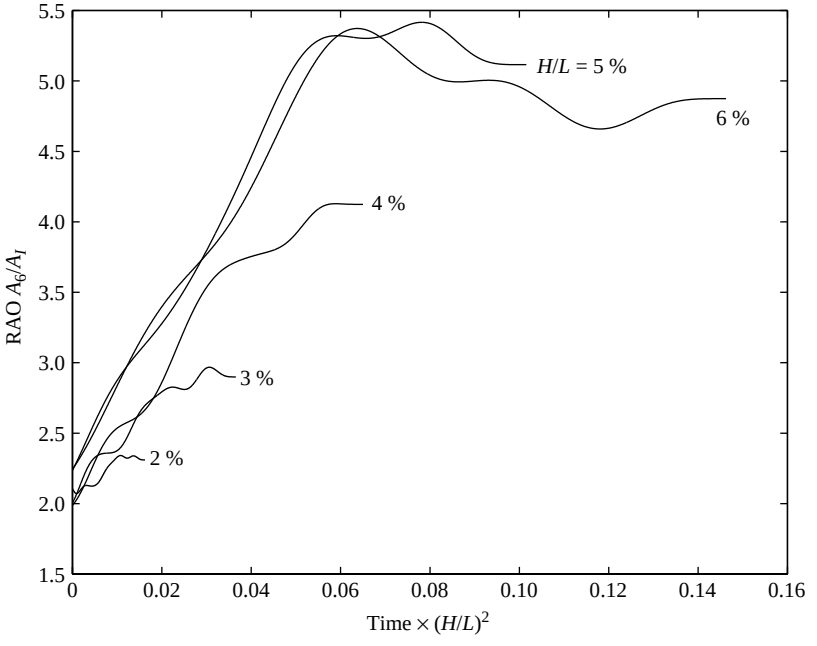

FIGURE 12. Time evolution of the RAO at gauge O6 (stretched time scale).
Wave period: 0.98 s.

The third-order analysis of Longuet-Higgins & Phillips (1962) shows that the wave-number of the first component is modified by a quantity $k_1^{(2)}$ given by

$$k_1^{(2)} = k^3 A_2^2 f(\beta) + \tfrac{1}{2} k^3 A_1^2 f(0) = k^3 A_2^2 f(\beta) - k^3 A_1^2, \tag{3.3}$$

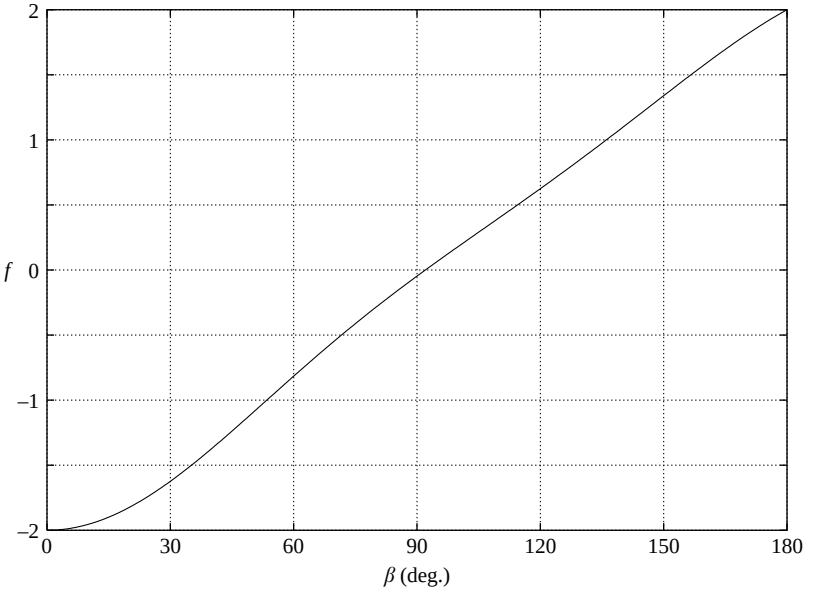

FIGURE 13. Interaction function f *vs.* angle β.

where the function $f(\beta)$ can be obtained from equation (2.8) of Longuet-Higgins & Phillips (1962) (with a factor 2 correction in the last line, see, e.g. Tanaka 2002) as

$$f(\beta) = -\left\{(1-\cos\beta)\,\sqrt{2+2\,\cos\beta} + 2\,\cos\beta + \tfrac{1}{2}\sin^2\beta + \frac{2\,(1-\cos\beta)}{\sqrt{2+2\,\cos\beta}-4}\,(1+\cos\beta+\sqrt{2+2\,\cos\beta})\right\}. \quad (3.4)$$

The function $f(\beta)$ is shown in figure 13.

In the case of a single wave ($A_2 \equiv 0$), we obtain $k_1^{(2)} = -k^3\,A_1^2$ which is the well-known wavenumber correction that arises in Stokes' third-order regular wave model: the wavelength increases. In a two-wave system, cross-interaction tends to decrease the wavelengths when the angle β is larger than 92°.

3.2. *Resolution of the linearized diffraction problem for the plate*

Because of the particular geometry of the experimental structure, the diffraction problem can be solved semi-analytically. Making reference to figure 14, we divide the fluid domain into two sub-domains, left and right of the plate, which are semi-infinite strips bounded by the tank walls. The incoming waves propagate from left to right, with amplitude A_I.

The problem is solved in the frequency domain:

$$\Phi(x, y, z, t) = \mathrm{Re}\,\{\varphi(x, y, z)\,\mathrm{e}^{-\mathrm{i}\,\omega t}\}.$$

In the left-hand-side sub-domain, the velocity potential can be expressed as

$$\varphi_1 = \frac{-\mathrm{i}\,A_I g}{\omega}\,\mathrm{e}^{kz}\left\{\mathrm{e}^{\mathrm{i}kx} + \sum_{n=0}^{N} B_n\,\mathrm{e}^{-\mathrm{i}\sqrt{k^2-\lambda_n^2}\,x}\,\cos\lambda_n y + \sum_{n=N+1}^{\infty} B_n\,\mathrm{e}^{\sqrt{\lambda_n^2-k^2}\,x}\,\cos\lambda_n y\right\}, \quad (3.5)$$

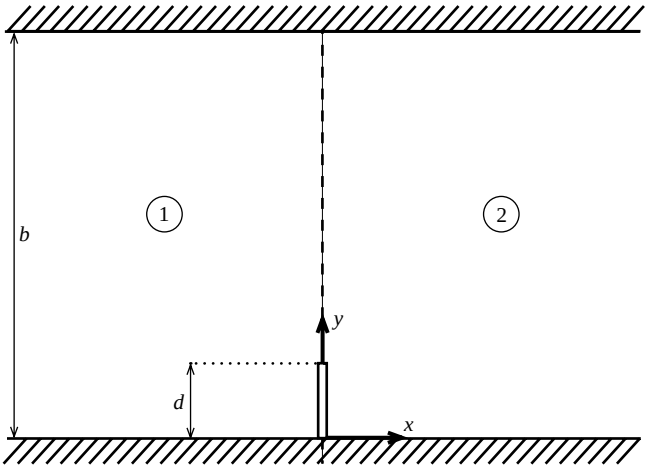

FIGURE 14. Geometry.

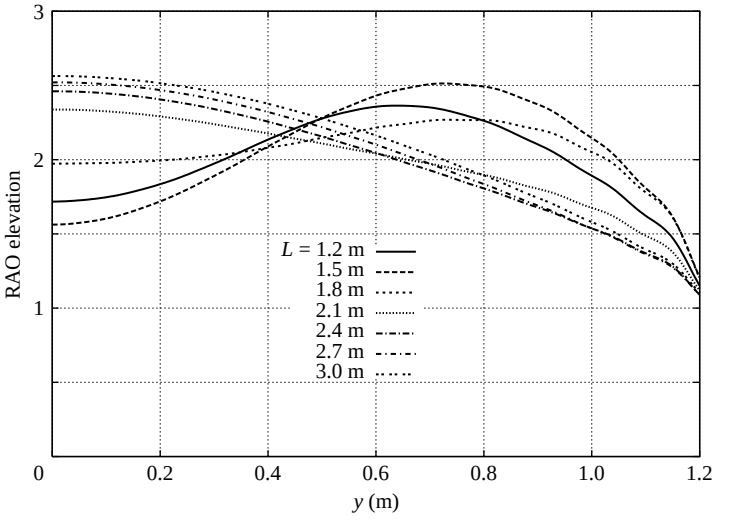

FIGURE 15. RAO of the free-surface elevation along the plate, for the different wavelengths.

and, in the right-hand-side sub-domain,

$$\varphi_2 = \frac{-\mathrm{i}\, A_I g}{\omega}\, \mathrm{e}^{kz} \left\{ \sum_{n=0}^{N} C_n\, \mathrm{e}^{\mathrm{i}\sqrt{k^2-\lambda_n^2}\, x}\, \cos \lambda_n y + \sum_{n=N+1}^{\infty} C_n\, \mathrm{e}^{-\sqrt{\lambda_n^2-k^2}\, x}\, \cos \lambda_n y \right\}. \qquad (3.6)$$

Here, $\lambda_n = n\,\pi/b$ and N is the largest integer n such that k is larger than λ_n. For $n \leqslant N$, the modes are progressive, for $n > N$, they are evanescent.

Equations (3.5) and (3.6) mean that the transmitted and reflected waves propagate to infinity without reflections from the beach or wavemakers.

The unknown coefficients B_n and C_n are determined by matching φ_1 and φ_2 (and their x derivatives) on the common boundary $x = 0$ for $d < y < b$ and by setting the no-flow condition on the plate. This gives a linear system that is solved with a standard Gauss routine.

Figure 15 shows the RAOs of the free-surface elevation along the plate, for the different wavelengths of the experimental tests. At the shortest wavelengths (1.2 m to

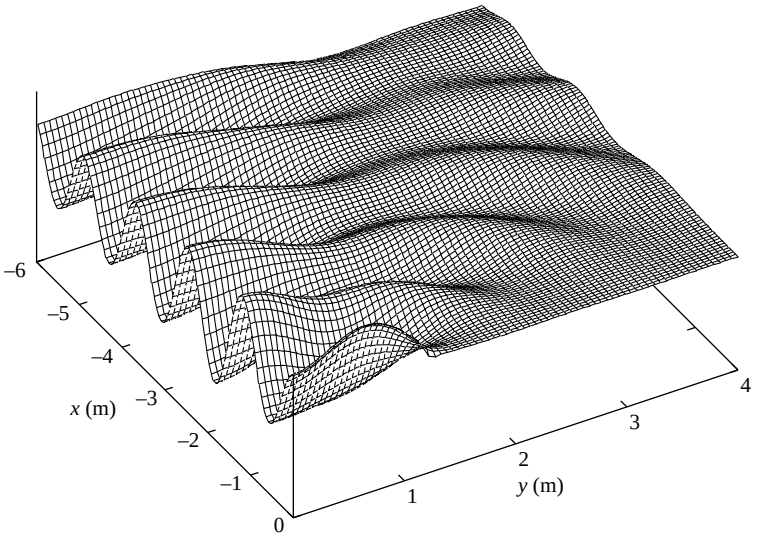

FIGURE 16. Three-dimensional view of the reflected wave field at a wavelength of 1.2 m.

1.8 m), the loci of the maximum elevation are not at the wall, but between the wall and the edge. At longer wavelengths, the RAOs are very similar, with a maximum value, at the wall, around 2.5.

Figure 16 is a bird's-eye view of the reflected wave field, at a wavelength of 1.2 m, in the immediate vicinity of the plate.

3.3. *Determination of the equivalent plane wave*

In order to be able to use Longuet-Higgins & Phillips' result for the modification of the wavenumber (equation (3.3)), we idealize, locally, the reflected wave system as a plane wave. This means that we identify, in the vicinity of the considered point, (x_0, y_0), the two expressions

$$A_I \sum_{n=0}^{N} B_n \, \mathrm{e}^{-\mathrm{i}\sqrt{k^2-\lambda_n^2}\,x} \cos \lambda_n y, \qquad A_R \, \mathrm{e}^{\mathrm{i}\,k\,[(x-x_0)\,\cos\beta+(y-y_0)\,\sin\beta]+\mathrm{i}\,\theta}. \tag{3.7}$$

This is achieved by equalizing the moduli (which gives A_R) and by taking the angle β as the direction of steepest variation of the first expression.

Figures 17 and 18 show the obtained amplitudes A_R (normalized by A_I) and angles β at different transversal cuts ahead of the plate (still at a wavelength of 1.2 m), over the first 6 m of the basin (in the transverse direction). They exhibit some waviness, which can be attributed to the confinement and some quasi-resonant transverse modes coming into play. It can be observed that the reflection is very strong along the wall, with normalized amplitudes A_R/A_I larger than 1.0 up to 4 wavelengths back.

3.4. *Modifications of the incoming waves owing to tertiary interactions with the reflected waves*

We now proceed to quantify the effects of tertiary interactions between the two wave systems. This means that we must allow for some space variation of the phase of the incoming waves and, as a consequence of the spatial variation of the reflected waves, of their amplitude as well.

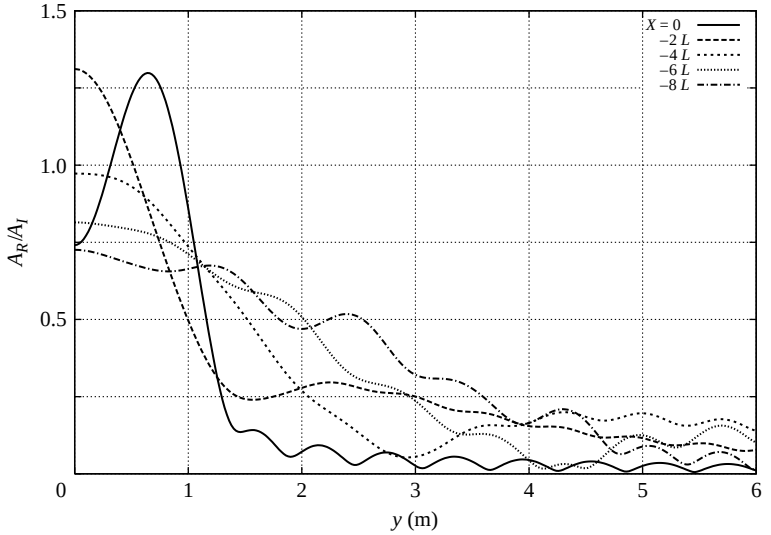

FIGURE 17. Equivalent plane wave. Obtained amplitudes A_R/A_I *vs.* y at increasing distances from the plate. Wavelength: 1.2 m; $b = 16$ m.

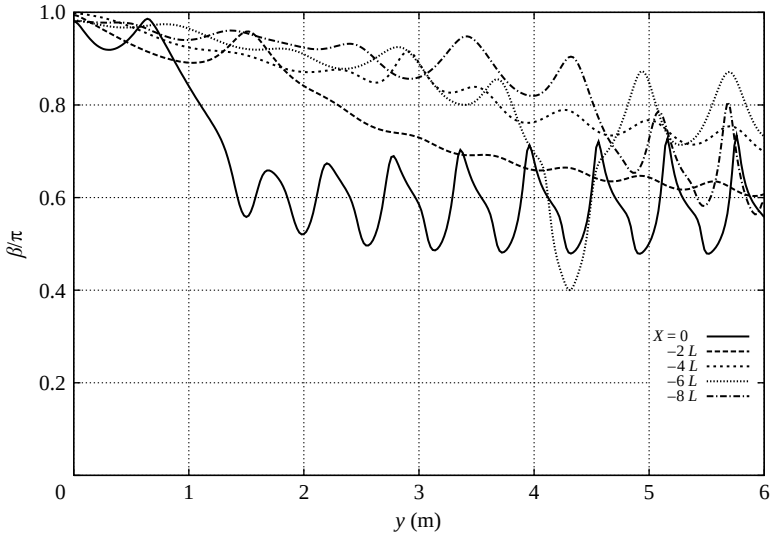

FIGURE 18. Equivalent plane wave. Obtained directions β *vs.* y at increasing distances from the plate. Wavelength: 1.2 m; $b = 16$ m.

We take the velocity potential of the incoming waves under the form

$$\varphi_I = \frac{-\mathrm{i}\,A(\varepsilon^2 x,\,\varepsilon y)\,g}{\omega}\;\mathrm{e}^{\mathrm{i}\,k\,(1-\varepsilon^2)\,x}\;\mathrm{e}^{\left[k+\varepsilon^2 k_1^{(2)}(\varepsilon^2 x,\varepsilon y)\right]\,z}, \tag{3.8}$$

where the complex amplitude A is assumed to vary slowly in x and y, at a rate that is related to the steepness $\varepsilon = k\,A_I$. The rate of variation in x is taken to be of the order ε^2, which is what would occur in a pure plane wave situation. In y, it is taken to be of order ε, as a result of the principle of least degeneracy. The same type of

variation arises in the parabolic approximation of the mild-slope equation, with the small coefficient ε being then related to the bottom slope (e.g. see Dingemans 1997).

It must be stressed here that the flow is still assumed to vary in time at the frequency ω, that is, we look for a steady-state solution and assume that such a steady-state solution exists.

The Laplace condition gives, to the order ε^2:

$$2\,\mathrm{i}k\,A_x + A_{yy} + 2k^4\,A_I^2\,A + 2k k_1^{(2)}\,A = 0, \tag{3.9}$$

or, from (3.3):

$$2\,\mathrm{i}k\,A_x + A_{yy} + 2k^4\,\left[A_R^2\,f(\beta) + A_I^2 - \|A\|^2\right]\,A = 0, \tag{3.10}$$

where $A_R(x, y)$ and $\beta(x, y)$ are the (real) amplitude and direction of propagation of the equivalent plane wave to the reflected field.

Taking

$$A = A_I\,(1+a), \qquad A_R = A_I\,a_R, \qquad \varepsilon = k\,A_I,$$

(3.10) can be rewritten as

$$2\,\mathrm{i}\,k\,a_x + a_{yy} + 2k^2\,\varepsilon^2\,\left[a_R^2\,f(\beta) + 1 - \|1+a\|^2\right]\,a = -2k^2\,\varepsilon^2\,\left[a_R^2\,f(\beta) + 1 - \|1+a\|^2\right]. \tag{3.11}$$

This equation is integrated in x and y, starting from $x = -l$ where it is assumed that $a(-l, y) = 0$. The choice of the distance l is discussed in § 3.6.

Advantage is taken of the confined geometry to expand $a(x, y)$ under the form

$$a(x, y) = \sum_{n=0}^{\infty} a_n(x)\,\cos\lambda_n y, \tag{3.12}$$

with $\lambda_n = n\pi/b$, as previously. This ensures that the no-flow condition at the walls $y = 0$ and $y = b$ is fulfilled.

It follows that the coefficients $a_n(x)$ satisfy

$$a_m' + \frac{\mathrm{i}\lambda_m^2}{2k}\,a_m - \frac{2\,\mathrm{i}\,k\,\varepsilon^2}{(1+\delta_{0m})\,b}\,\sum_{n=0}^{\infty}\left[\int_0^b \left[a_R^2\,f(\beta) + 1 - \|1+a\|^2\right]\,\cos\lambda_m y\,\cos\lambda_n y\,\mathrm{d}y\right]a_n$$
$$= \frac{2\,\mathrm{i}\,k\,\varepsilon^2}{(1+\delta_{0m})\,b}\,\int_0^b \left[a_R^2\,f(\beta) + 1 - \|1+a\|^2\right]\,\cos\lambda_m y\,\mathrm{d}y \tag{3.13}$$

(δ_{0m} being the Kronecker symbol),
or, under vectorial form:

$$\boldsymbol{a}'(x) + \boldsymbol{M}(x, \boldsymbol{a}(x))\cdot\boldsymbol{a}(x) = \boldsymbol{b}(x, \boldsymbol{a}(x)), \tag{3.14}$$

where the matrix $\boldsymbol{M}$ and the vector $\boldsymbol{b}$ depend on $\boldsymbol{a}(x)$.

The x-integration is carried out according to the second-order implicit scheme

$$\boldsymbol{a}'(x) \simeq \frac{3\,\boldsymbol{a}(x) - 4\,\boldsymbol{a}(x-\Delta x) + \boldsymbol{a}(x-2\,\Delta x)}{2\,\Delta x}, \tag{3.15}$$

yielding the linear system

$$[3\,\boldsymbol{I} + 2\,\Delta x\,\boldsymbol{M}(x, \boldsymbol{a}(x))]\cdot\boldsymbol{a}(x) = 2\,\Delta x\,\boldsymbol{b}(x, \boldsymbol{a}(x)) + 4\,\boldsymbol{a}(x-\Delta x) - \boldsymbol{a}(x-2\,\Delta x). \tag{3.16}$$

This is solved iteratively, the matrix $\boldsymbol{M}$ and the vector $\boldsymbol{b}$ being updated at each iteration (two iterations suffice in practice, starting from the values at $x - \Delta x$).

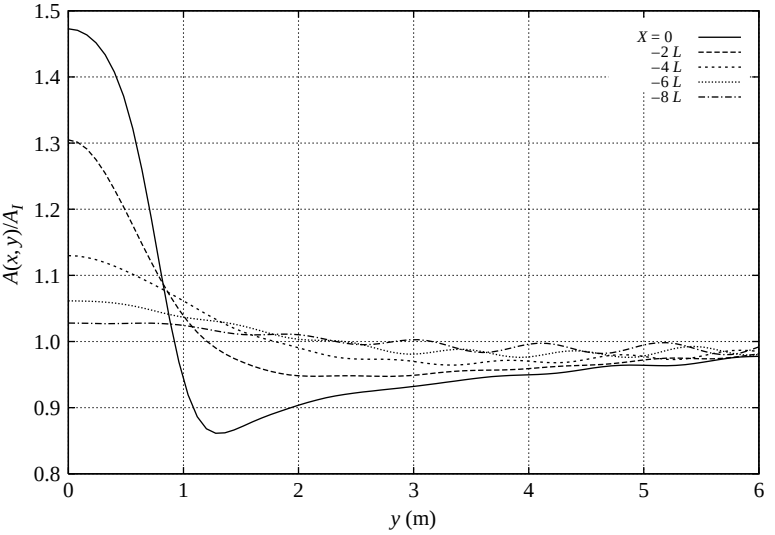

FIGURE 19. Incoming-wave amplitude ahead of the plate. Period: 0.88 s, steepness H/L: 4 %.

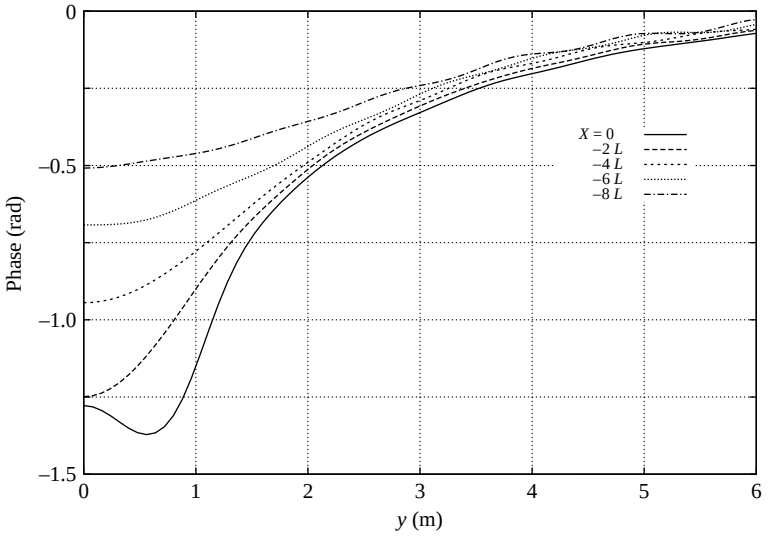

FIGURE 20. Phase of the incoming wave ahead of the plate. Period: 0.88 s, steepness H/L: 4 %.

Figures 19 and 20 show the amplitudes and phases obtained in the case of a period of 0.88 s and a steepness H/L of 4 % ($k\,A_I \simeq 0.13$). The calculations start 19.3 m ahead of the plate (the distance from the wavemakers to the plate), that is 16 wavelengths. The amplitudes and phases are given along transverse cuts at 8, 6, 4, 2 and 0 wavelengths from the plate.

3.5. *New resolution of the diffraction problem*

It is quite easy to solve again the diffraction problem with the modified incoming-wave field. In the left-hand side of the domain (see figure 14) the velocity potential is

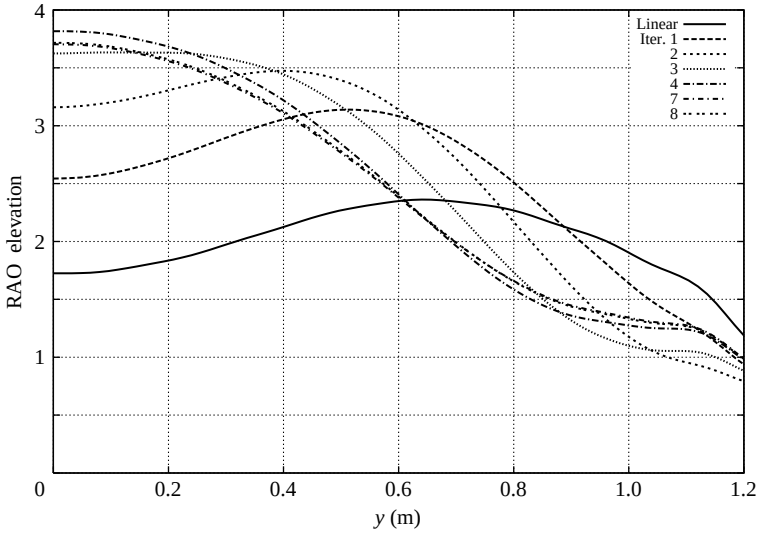

FIGURE 21. Evolution of the RAO of the free-surface elevation through the iterations. Period: 0.88 s, steepness H/L: 4 %.

now written

$$\varphi_1 = \frac{-\mathrm{i}\ A_I\, g}{\omega}\ \mathrm{e}^{kz}\ \sum_{n=0}^{\infty}[(a_n + \delta_{n0})\ \mathrm{e}^{\mathrm{i}kx} + B_n\ \mathrm{e}^{-\mathrm{i}\alpha_n x}]\ \cos\lambda_n y, \tag{3.17}$$

while in the right-hand side sub-domain it is taken under the same form as before:

$$\varphi_2 = \frac{-\mathrm{i}\ A_I\, g}{\omega}\ \mathrm{e}^{kz}\ \sum_{n=0}^{\infty} C_n\ \mathrm{e}^{\mathrm{i}\alpha_n x}\ \cos\lambda_n y. \tag{3.18}$$

The diffraction problem being solved, we may return to the previous step of calculating the modifications of the incoming waves, under tertiary interaction with the updated reflected field. The diffraction problem can be solved again, etc., and this process repeated until convergence is reached (if ever).

In figure 21 the evolution of the RAO of the free-surface elevation along the plate is shown (still in the case of a wave period equal to 0.88 s and a steepness H/L of 4 %). It can be seen that the point of maximum elevation, initially in $y \simeq 0.6$ m, moves to the wall. After a few iterations, convergence is reached with a value of the RAO, at the wall, around 3.7 (more than twice the linear value).

In figure 22, we present analogous results to figure 19, at the end of the iterations. As compared to this figure, it can be observed that the amplitude has increased by the plate–wall intersection: it is now nearly twice the initial amplitude.

Similarly, in figure 23, the phase angles obtained after convergence are shown. Referring to figure 20, it can be observed that the angles have increased (in absolute values) and have become comparable with the experimental ones (see figure 5).

Finally, figure 24 gives a bird's eye view of the incident wave field in the vicinity of the plate. The shortening of the wavelength, and the increase of the amplitude along the wall can clearly be seen.

Figure 25 gives the final RAOs obtained after convergence, still in the case of a 0.88 s period, for steepnesses ranging from 2 to 6 %. To achieve convergence at

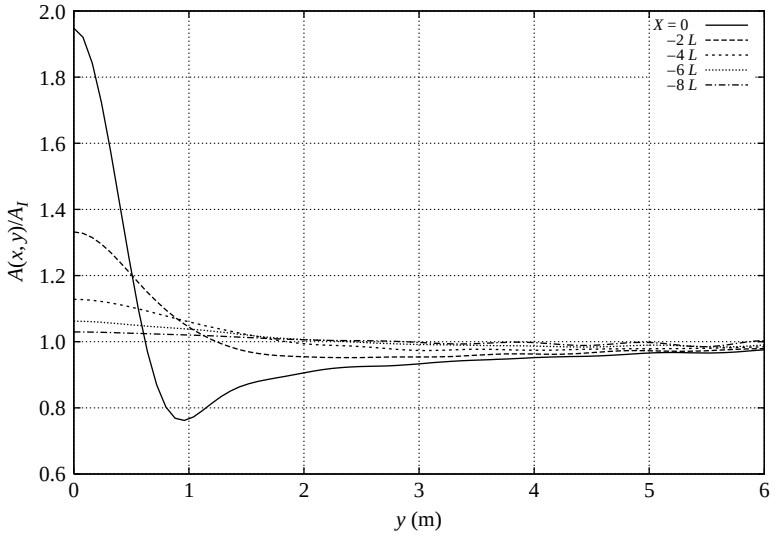

FIGURE 22. Incoming-wave amplitude at end of iterations. Period: 0.88 s, steepness H/L: 4 %.

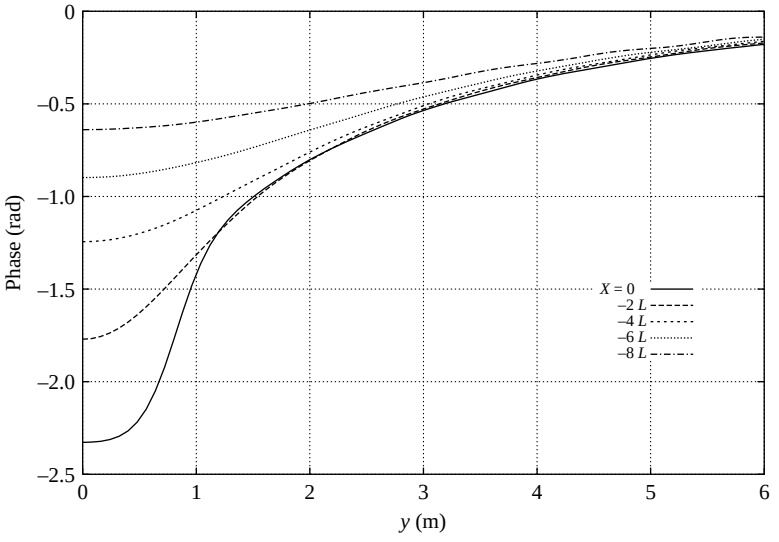

FIGURE 23. Phase angle of the incoming waves at the end of the iterations. Period: 0.88 s, steepness H/L: 4 %.

the two highest steepnesses, it was necessary to introduce some relaxation into the iterative scheme.

3.6. *Sensitivity to the interaction distance*

To produce the results shown in figures 19 to 25, we have integrated (3.10), starting from $x = -l = -19.3$ m, with $A(-l, y) = A_I$ as the initial value. This abscissa corresponds to the location of the wavemakers.

At 4 % steepness, we have repeated the calculations for different interaction lengths l, ranging from twice to 64 times the wavelength L. The final RAOs obtained are shown in figure 26. Quasi-identical curves are obtained at the longer lengths of 32 and

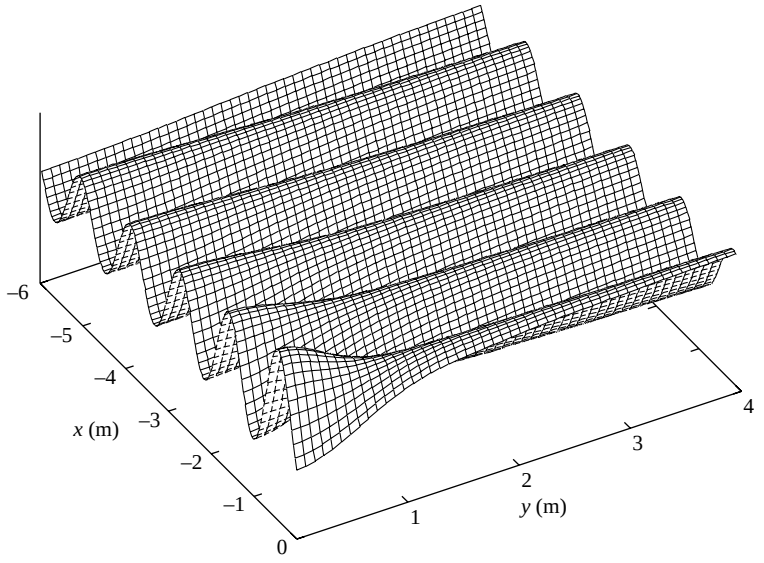

FIGURE 24. Three-dimensional view of the incoming waves by the plate. Period: 0.88 s, steepness H/L: 4 %.

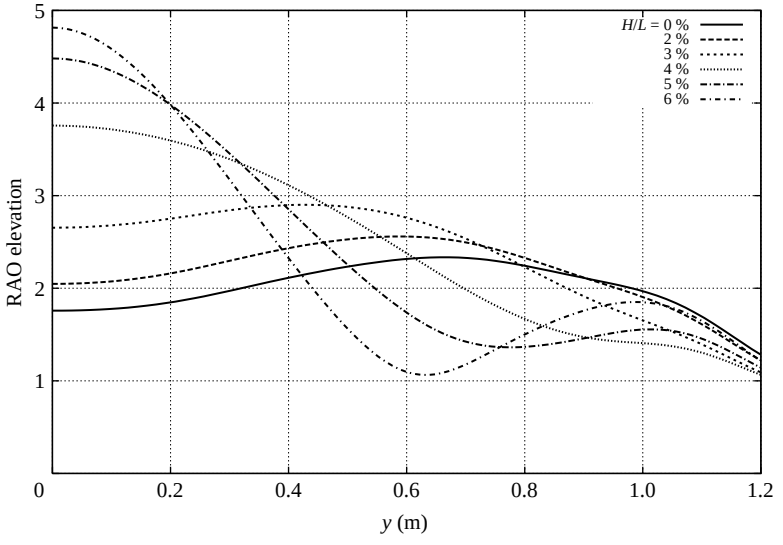

FIGURE 25. RAOs of the free-surface elevation at different steepnesses. Period: 0.88 s.

64 wavelengths, with the same maximum value of 4.0 at the plate–wall intersection. At 16 wavelengths ($l = 19.3$ m), slightly lower values are obtained. This suggests that the plate was too close to the wavemakers for this particular wave period.

It must be pointed out here that the far-field behaviour of the reflected waves in the basin has nothing to do with their far-field behaviour in the open ocean: in the basin, because of the confinement in between the walls, the amplitude of the reflected waves does not go to zero at infinity, but ends up spreading out more or less equally over the width of the basin (for a large number of propagating modes). In an infinite

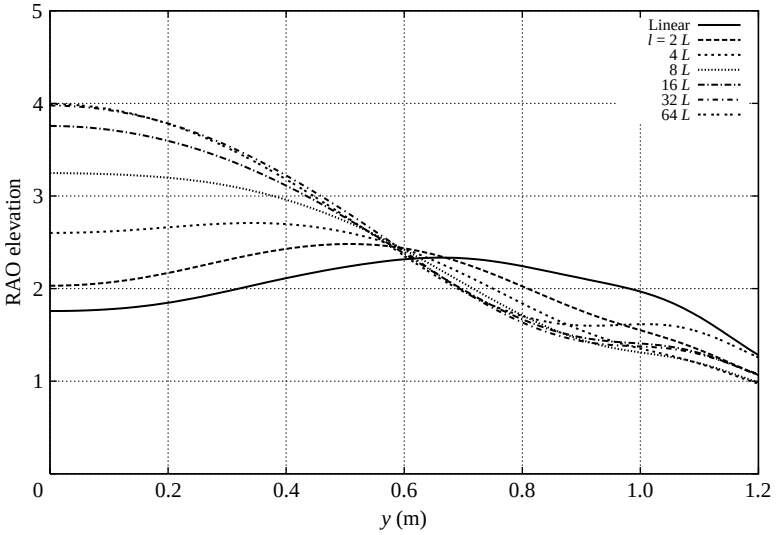

FIGURE 26. Effect of the interaction distance. Period: 0.88 s, steepness H/L: 4 %.

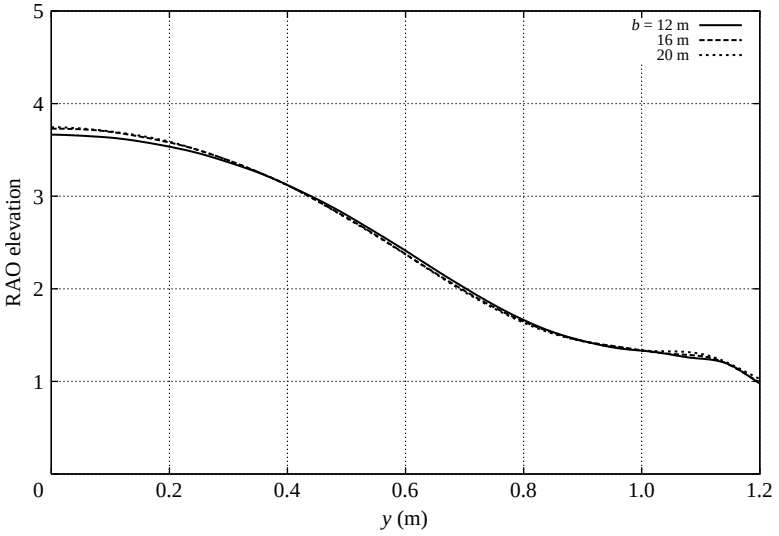

FIGURE 27. Effect of varying the basin width. Period: 0.88 s, steepness H/L: 4 %, integration length: 19.3 m.

ocean, it decays as $1/\sqrt{R}$, where R is the distance from the plate. This raises the problem of confinement effects for the phenomena that we are studying here.

To check whether the basin width plays an important role, we carried out calculations, in the case $l = 16L$, for two other widths of 12 and 20 m. The results are shown in figure 27, where it appears that the differences are very small. So the finite width of the basin does not appear to be of much concern, at least in this particular case.

Figure 28 shows similar results to figure 26, in the case of a wave period of 1.24 s, meaning a wavelength of 2.4 m, twice the previous value. The steepness H/L is kept the same, that is 4 %. It can be seen that the RAOs coalesce together at interaction lengths larger than some value in between 4 and 8 wavelengths, meaning a shorter

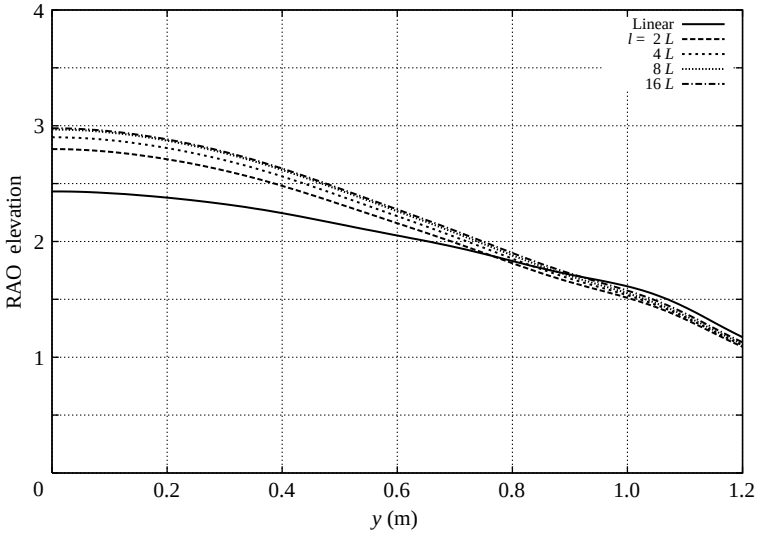

FIGURE 28. Effect of the interaction distance. Period: 1.24 s, steepness H/L: 4 %.

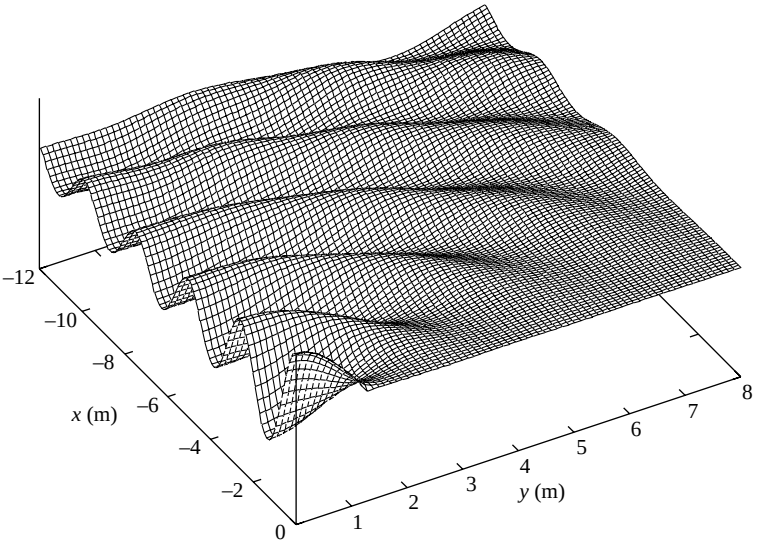

FIGURE 29. Three-dimensional view of the reflected wave field at a wavelength of 2.4 m.

distance than in the previous case. This is because the reflected wave system is much less focused along the longitudinal wall (see figure 29). Correlatively, the number of iterations necessary to achieve convergence decreases.

4. Further experimental results and comparison with calculated values

In this section we present further experimental results, interpret them and make comparisons with our simplified model.

Our understanding of the observed phenomena is the following: the wavemakers being activated, the incoming wave system propagates in the basin, at the group velocity C_G, with a modulation and steepening of the wavefront (according to theory),

and starts interacting with the plate. A reflected wave system is produced that propagates back toward the wavemakers, also at the group velocity. The two wave systems interact over an area increasing in time at the rate C_G and modify each other. This means that the incoming waves are undergoing continuous evolution, until a state of equilibrium is eventually reached, if there is one. Unfortunately, in the basin, time is limited as the reflected waves re-reflect on the wavemakers, meaning that the exploitable part of the tests is less than twice the distance, from the plate to the wavemakers, divided by the group velocity, as argued before.

4.1. *Rate of change of phase lag*

The quasi-linear time variation of the phase angle of the free-surface elevations, at the plate, can be related to the linear rate of increase of the interaction area, as can be easily seen in a two-dimensional situation: assuming, for the sake of simplicity, that the incoming and reflected wave systems propagate as step functions, the free-surface elevation, in between the wavemakers and the plate, is given by

$$\eta(x,t) = A_I\, H(C_G\, t - x)\, \cos(kx - \omega t + \theta_I) + A_R\, H(C_G\, t + x)\, \cos(kx + \omega t + \theta_R), \quad (4.1)$$

with H the Heaviside function and $t = 0$ the instant when the incoming waves reach the plate.

Cross-interaction between the incoming and reflected waves results in a phase delay of the incoming waves, at the plate, given by

$$\psi(t) = -2\, k^3\, A_R^2 \int_{-C_G\, t}^{0} \mathrm{d}x = -k^2\, A_R^2\, \omega\, t. \quad (4.2)$$

Assuming $A_R \sim A_I$, equation (4.2) gives $L^2/H^2\, \mathrm{d}\psi/\mathrm{d}t = -\pi^2\, \omega$, that is $-70\,\mathrm{rad\,s^{-1}}$ for the shortest wave period of 0.88 s, while figure 8 shows a slope of about $-40\,\mathrm{rad\,s^{-1}}$. The discrepancy can presumably be attributed to three-dimensional effects and to the modulations of the wavefronts.

4.2. *Modifications of the incoming wave amplitude ahead of the plate*

To investigate whether the amplitude of the incoming waves does change prior to reaching the plate, we analyzed the time records of the free-surface elevations measured at gauges S5 to S10, ahead of the plate. We considered them in pairs, that is (S8–S5), (S9–S6) and (S10–S7), and used a two-gauge method to separate incoming and reflected waves, assumed both to propagate in the x-direction and to have constant amplitudes from one gauge to the other (the separation distance being 50 cm). To properly separate both components, it turned out to be necessary to take account of the modifications of the wave numbers, due to self and cross-interactions. That is the free-surface elevation is written

$$\eta(x, y, t) = A_I\ \cos(k_I\, x - \omega\, t + \theta_I) + A_R\ \cos(k_R\, x + \omega\, t + \theta_R), \quad (4.3)$$

where

$$k_I\ =\ k + 2\, k^3\, A_R^2 - k^3\, A_I^2, \quad (4.4)$$

$$k_R\ =\ k + 2\, k^3\, A_I^2 - k^3\, A_R^2, \quad (4.5)$$

meaning that the wavenumbers depend (weakly) on the unknown amplitudes A_I and A_R. This difficulty is overcome through an iterative scheme.

Results are given in figure 30, again in the case $T = 0.88$ s, $H/L = 4\,\%$. It shows the time evolution of the amplitude of the incoming waves, at the three locations, as determined over sliding windows three wave periods long. The amplitude of the waves

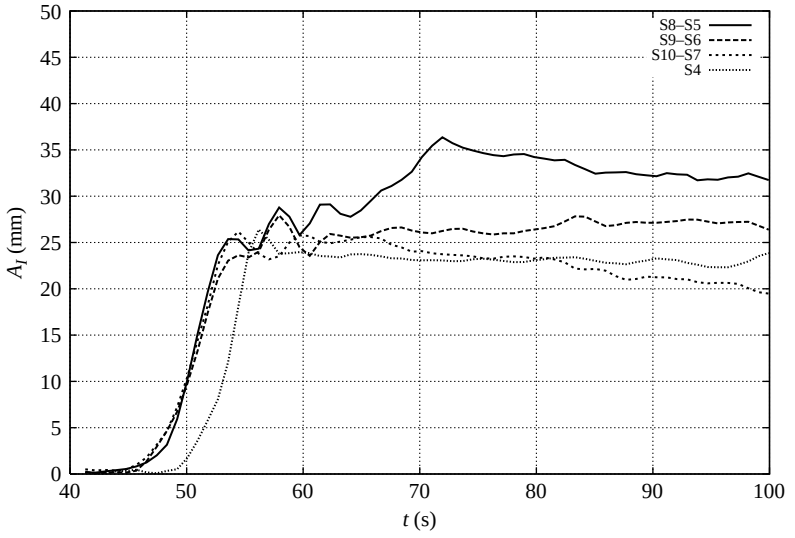

FIGURE 30. Time evolution of the amplitude of the incoming waves in between gauges (S8–S5), (S9–S6), (S10–S7) and away from the plate (S4). Period: 0.88 s, steepness H/L: 4 %.

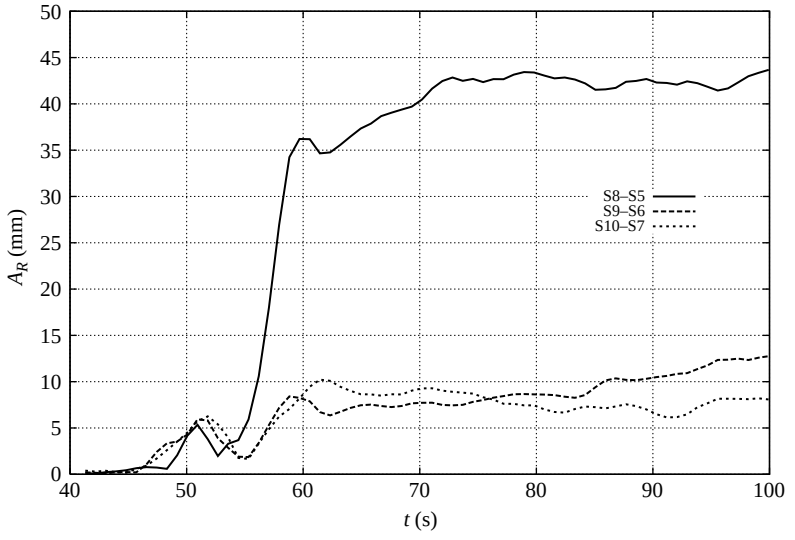

FIGURE 31. Time evolution of the amplitude of the reflected waves in between gauges (S8–S5), (S9–S6), (S10–S7). Period: 0.88 s, steepness H/L: 4 %.

away from the plate, at gauge S4, is also shown. A strong increase of the incoming wave amplitude, in between gauges S8 and S5 (at 2 m from the plate), can clearly be seen, up to 1.5 times the reference value given by S4. The ratio then decreases to around 1.4, in fair agreement with the value (1.35) provided in figure 22 at 2.4 m ($2\,L$) from the plate. The slight decrease in time of the incoming wave amplitude in between gauges S10 and S7, 2.1 m away from the wall, can also be noticed, in qualitative agreement with figure 22.

Figure 31 shows, for the same test, the time evolution of the amplitude of the reflected waves, at the same locations. It should be noted that, in figures 30 and 31,

the time reference is not the arrival of the wavefront at the plate but the beginning of data acquisition.

4.3. *Comparison between measured and calculated free-surface elevations along the plate*

As outlined before, the main difficulty in this comparison is associated with the fact that our theoretical model expresses the steady-state solution, whereas in many tests no steady state is apparently reached within the exploitable time window.

In figures 32 to 36 we present experimental and numerical RAOs of the free-surface elevation along the plate, at wave periods of 0.88, 0.98, 1.07, 1.16 and 1.39 s. The experimental RAOs are derived from the measured elevations over a time window of three periods just before re-reflected waves reach the plate. They are drawn as straight segments joining the values obtained at the gauges O1 to O6, therefore starting at $y = 0.1$ m and ending at $y = 1.0$ m. In each figure, the top part shows the time evolution of the RAO at gauge O6 for the different steepnesses, as derived from the experimental record.

As already mentioned, at 0.88 s wave period and 6 % steepness, the standing-wave system quickly becomes too steep and begins to break, dissipating energy. This is reflected in the time evolution of the RAO at gauge O6 (figure 32*a*) that drops down after attaining values around 4.5. For this reason, no comparison can be made with calculated values. Still at the 0.88 s period, it clearly appears in the same figure that the 2, 3 and 4 % curves have not reached horizontal asymptotes within the allowable time window. As a result, it is difficult to make meaningful comparisons between calculated and measured RAOs along the plate.

At the 0.98 s period (figure 33), breaking also occurs at 6 % steepness. At the lower steepnesses, the gauge O6 RAOs seem to have reached steady values by the end of the time traces and fair agreements are obtained between computed and measured RAOs along the plate. Reasonably good agreements can also be seen at the other wave periods. At the highest one (1.39 s), the run-up effect becomes much weaker, but both experiments and calculations agree over a 35 % increase of the RAO peak over linear calculations (at the highest steepness), which is far from negligible for air-gap calculations.

Noticeable in some of the plots of the time evolution of the RAO at gauge O6 are oscillations, particularly at the 1.16 s period (figure 35). They are also visible in figures 5 and 7 showing the time evolution of the phase lags, with the same period around 13 s whatever the steepness. Presumably they are associated with the first longitudinal mode of the tank that becomes excited during the wave generation phase (Molin 2001).

5. Final comments

We believe that we have provided sufficient evidence that our interpretation of the observed experimental phenomena is correct: the strong run-up effects are due to tertiary interactions between the incoming waves and the reflected wave field, over a wide area on the weather side of the plate. These interactions slow down the incoming waves, like a shoal, and induce focusing toward the centre of the plate. Even though, in the cases of ships and barges, these run-ups had been observed for a long time (Pinkster, personal communication 2003), it looks as if no satisfactory explanation has been given so far.

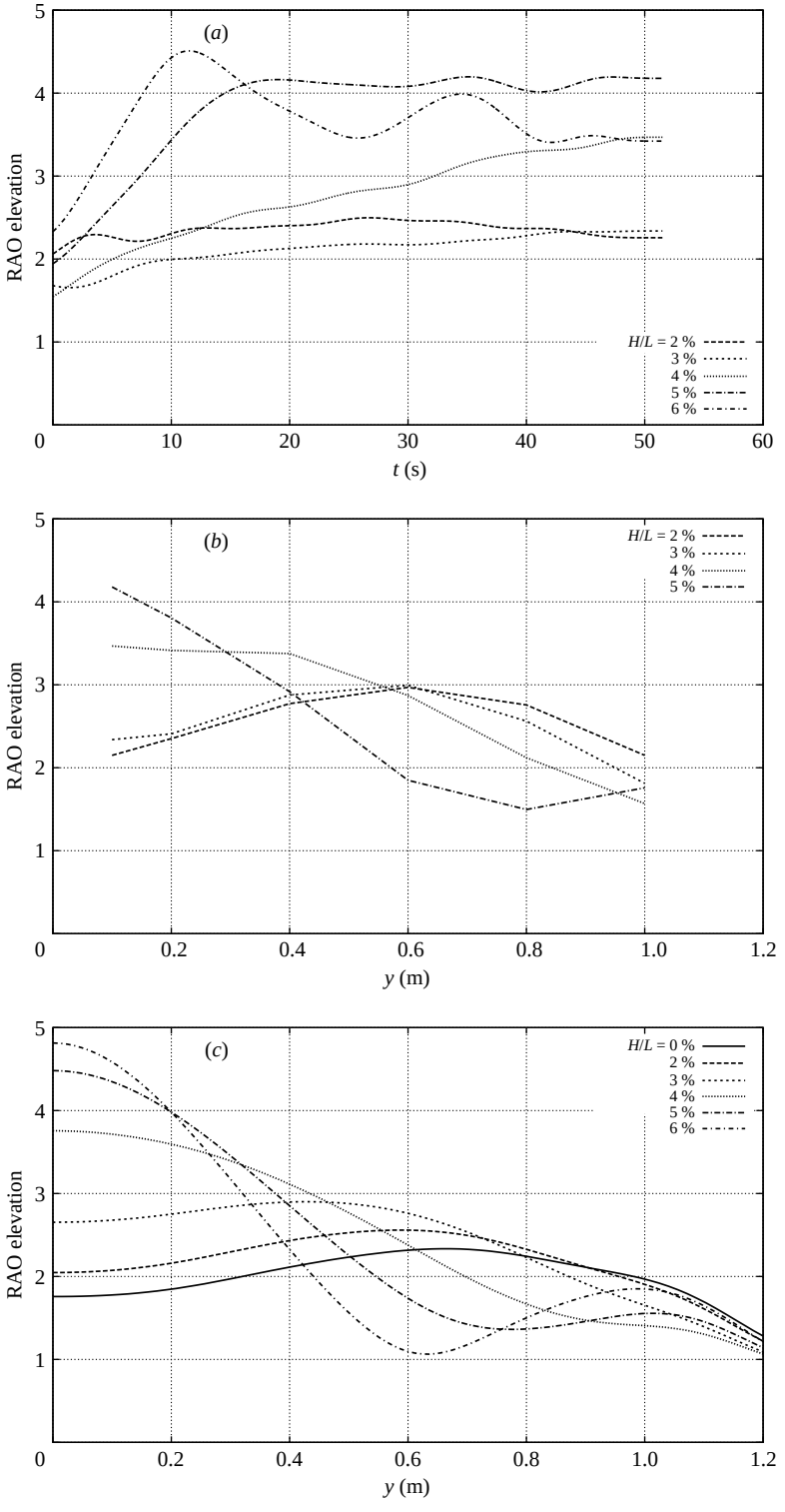

FIGURE 32. (*a*) Time evolution of the RAO of the free-surface elevation at gauge O6. (*b*) Measured and (*c*) calculated RAOs along the plate. Period: 0.88 s.

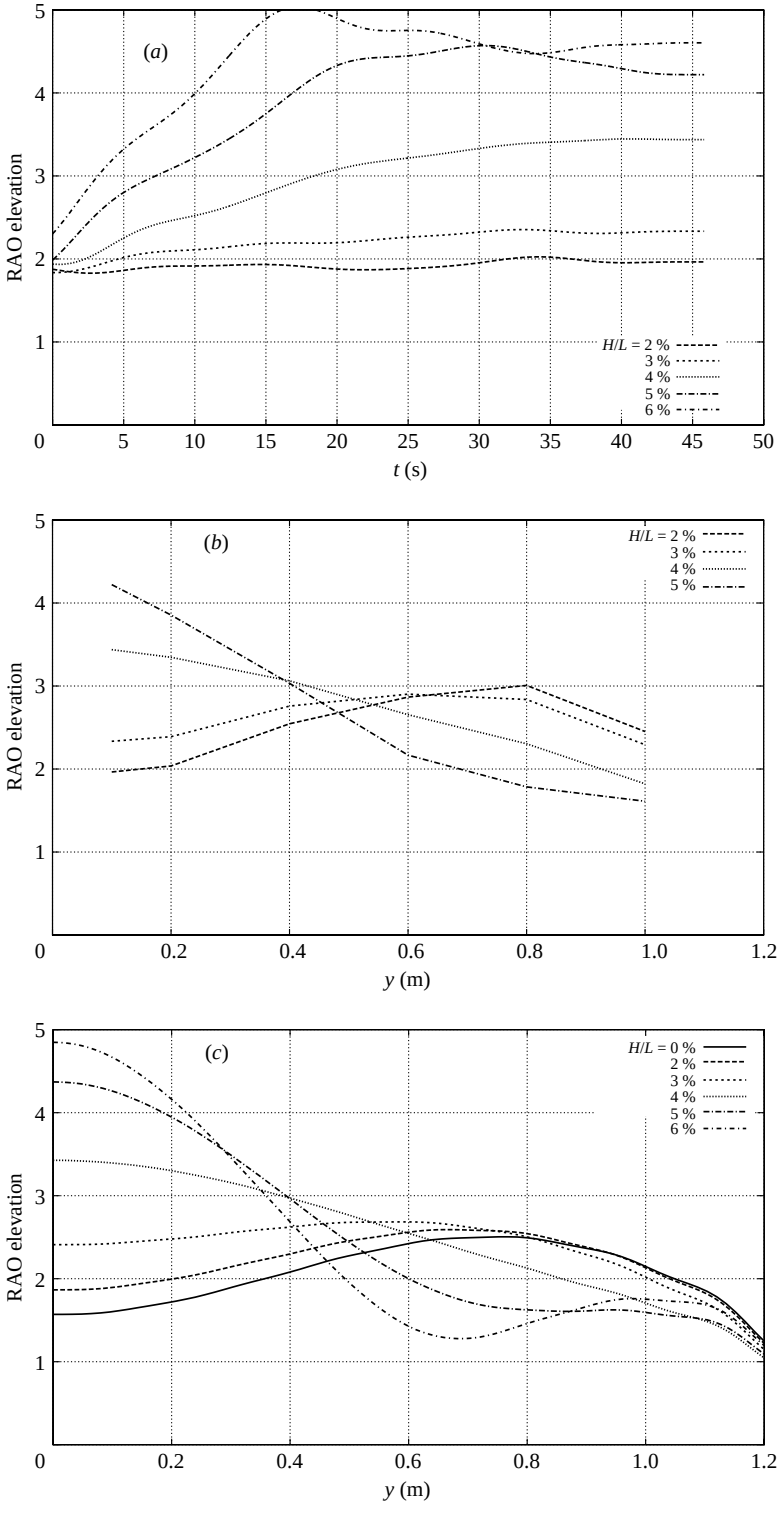

FIGURE 33. As figure 32. Period: 0.98 s.

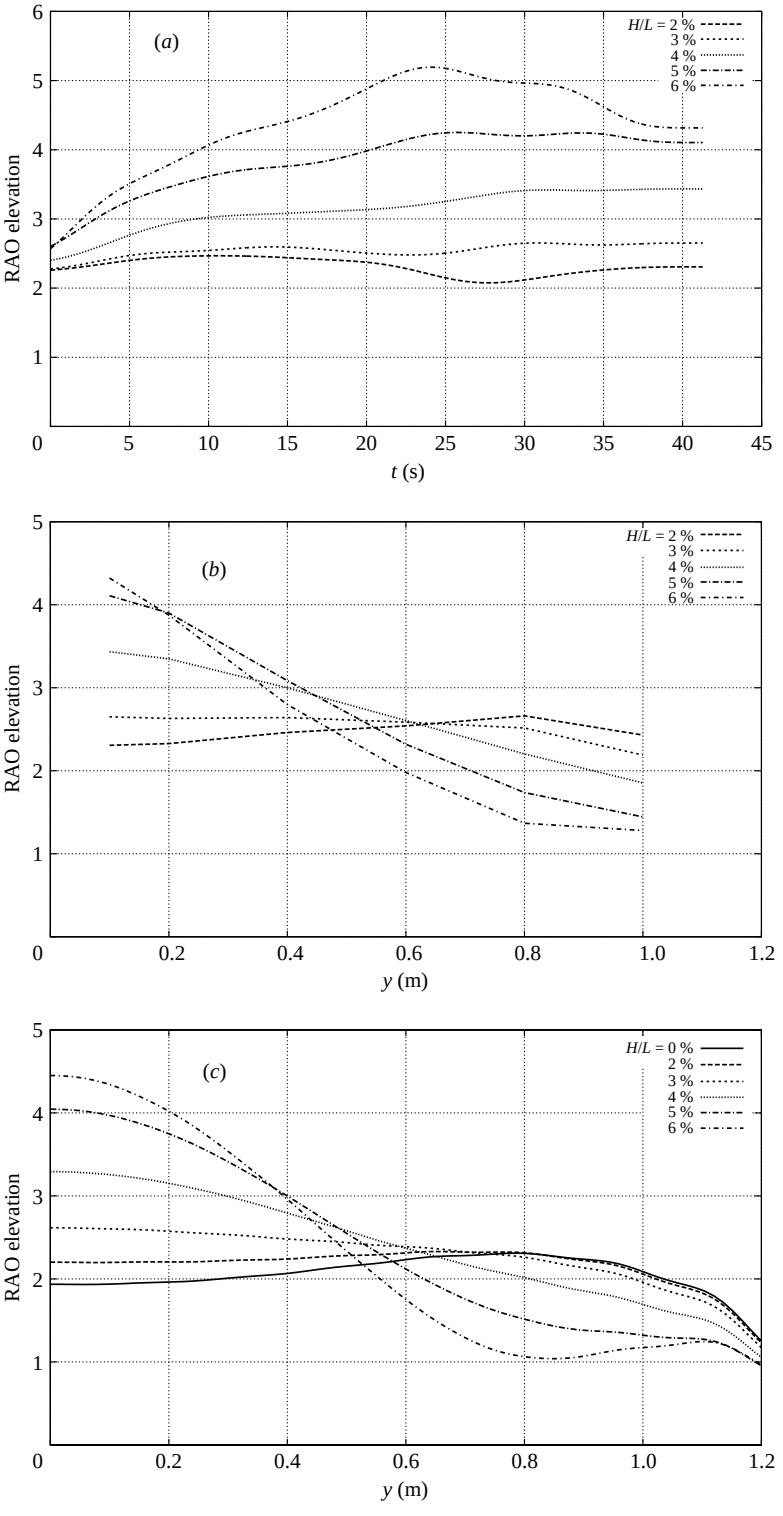

FIGURE 34. As figure 32. Period: 1.07 s.

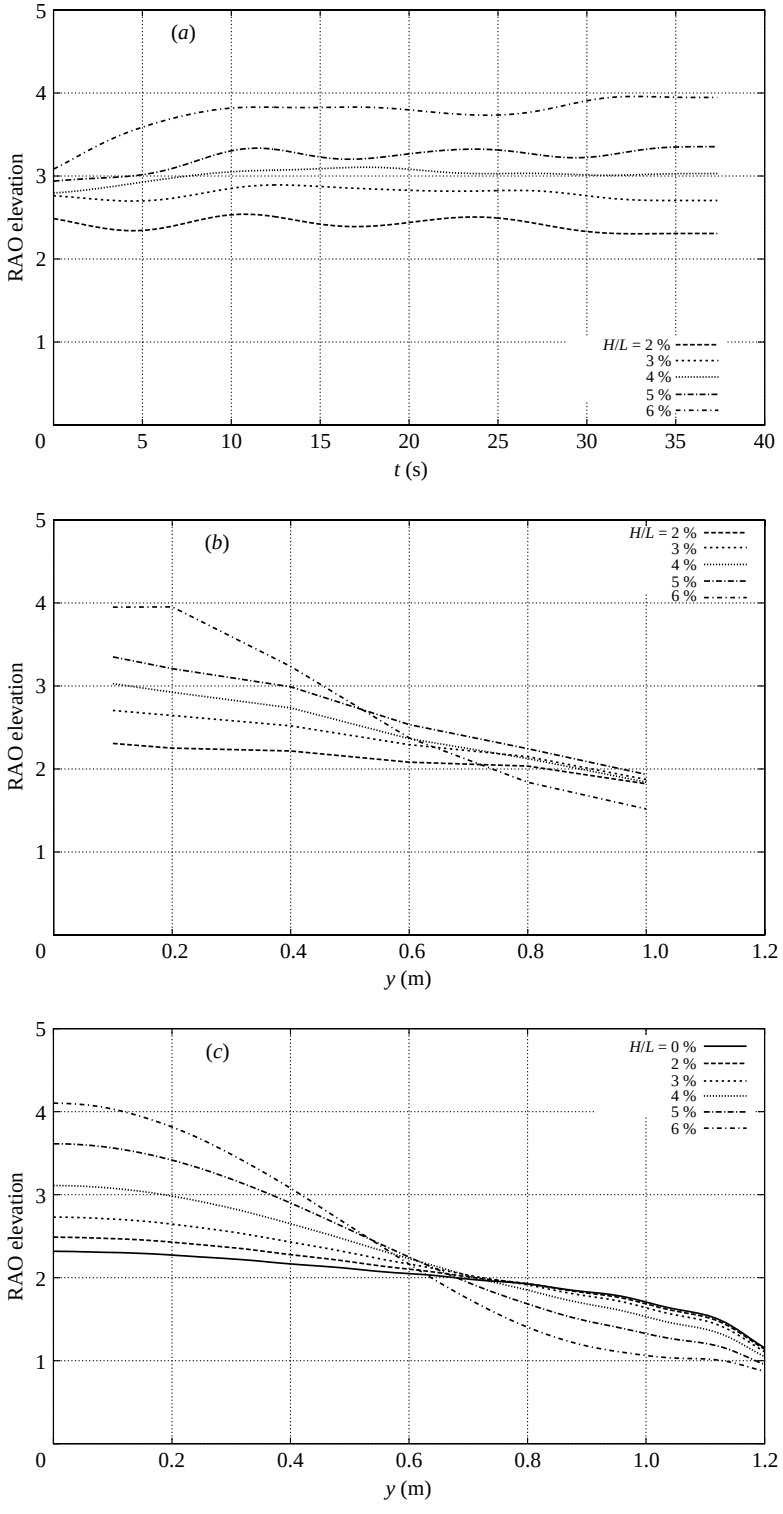

FIGURE 35. As figure 32. Period: 1.16 s.

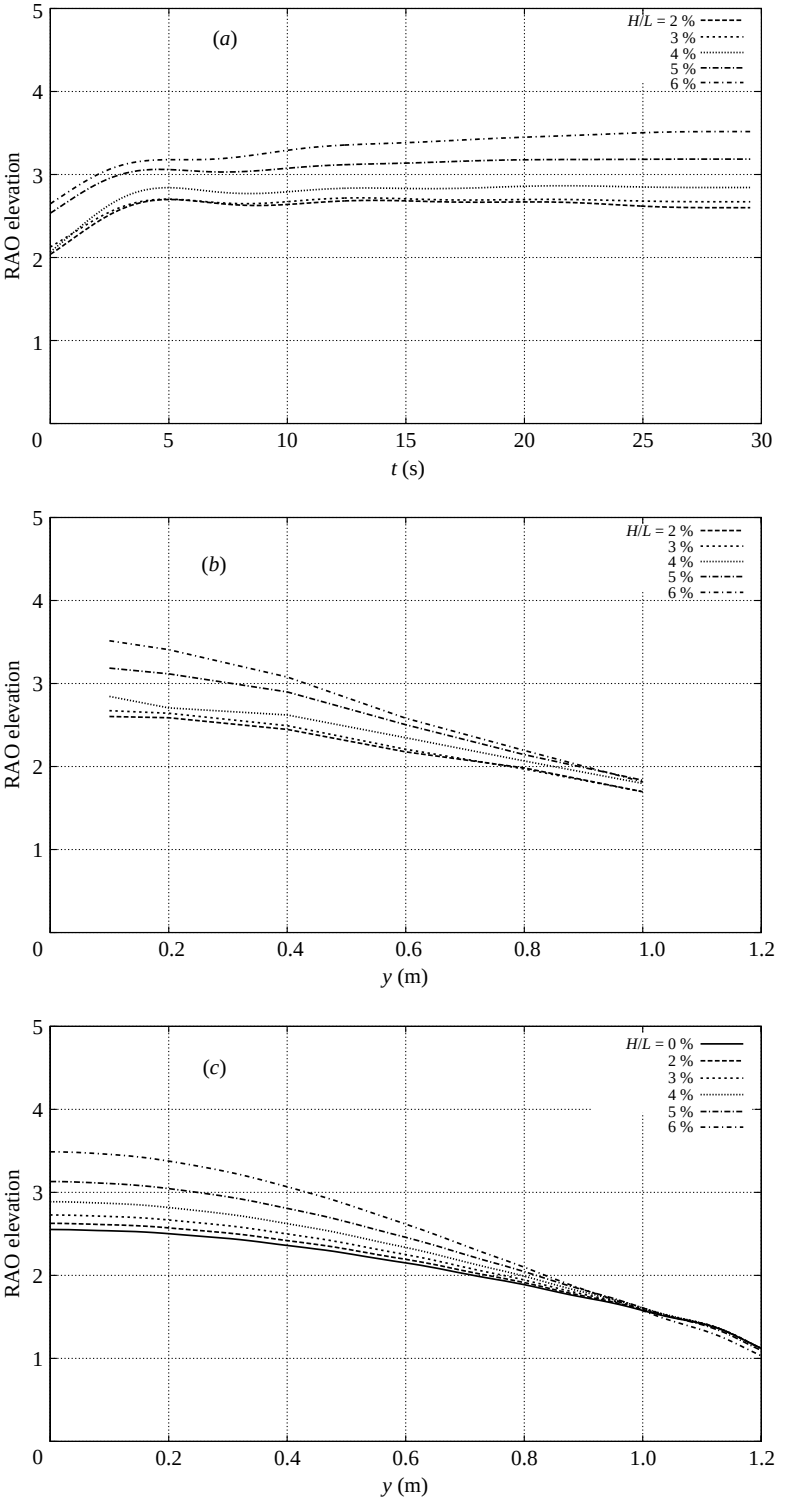

FIGURE 36. As figure 32. Period: 1.39 s.

We have proposed a theoretical model that seems to reflect the physics correctly. However, it can be criticized in many respects:

(i) the plane wave approximation applied to the reflected wave field needs further justification;

(ii) the hypothesis that the amplitude of the incoming waves varies slowly in the transverse direction is not strictly fulfilled (see, for instance, figure 22);

(iii) modifications of the reflected wave system, through tertiary interactions with the incoming one, are not considered;

(iv) the problem is solved in the frequency domain, on the basis that a steady-state solution exists.

Concerning this last point, the model tests did not give evidence that steady states were always attained. The main reason seems to be related to the fact that the exploitable time window is limited by the multiple reflections in between the plate and the wavemakers. At short wavelengths, where the interaction area extends far away from the plate, the duration of the transients is too long for a steady state to be attained within the allowable time window.

It would certainly be instructive to make comparisons with results from fully nonlinear time domain numerical models. The numerical challenge is that a wide domain must be covered; the shorter the wavelength (with regards to the size of the body), the larger the computational domain must be. A promising route seems to be the enhanced Boussinesq equations first proposed by Agnon, Madsen & Schäffer (1999) and Madsen, Bingham & Liu (2002), and further developed by Fuhrman & Bingham (2004). Preliminary results have already been obtained, with excellent agreement with the experimental records (Bingham *et al.* 2004).

The practical implications of these findings are obvious for the survival of disabled barges or ships, in beam seas. As a matter of fact, our first experience with this run-up phenomenon was when doing model tests on the rolling motion of barges (from which figure 1 has been taken). The barge model started shipping large amounts of water and the test program had to be revised to milder sea-states. Associated with these run-up and water-shipping effects are high local loads that are likely to induce damage to the structure. This could have been a key mechanism in the loss of some ships like the Prestige (Rainey, personal communication 2004). Other cases of concern are multi-legged offshore structures, that have been known to suffer from air-gap problems (e.g. see Swan, Taylor & van Langen 1997, or Mavrakos *et al.* 2004), and coastal structures, such as breakwaters, or the planned GBS (gravity base structures) for LNG storage and off-loading.

A lot more theoretical and numerical work remains to be done, such as tackling the cases of finite depth, irregular waves and non-normal incidence. The theoretical model that we have proposed can easily be extended to these issues.

The model tests at BGO-First were carried out within the Gis-Hydro organization, with financial support from Conseil Général du Var. The analysis was done as part of a CLAROM research project on 'run-up'. Partners in the project are Principia RD, Bureau Veritas, Doris Engineering, ESIM, Saipem SA and Sogreah. Preliminary results were given at the Eighteenth International Workshop on Water Waves and Floating Bodies (Molin *et al.* 2003) and at the Cinquième Rencontre Hydrodynamique Marine 2004 (Molin 2004). Further results from the experiments can be found in Molin *et al.* 2004.

REFERENCES

Agnon, Y., Madsen, P. A. & Schäffer, H. A. 1999 A new approach to high-order Boussinesq models. *J. Fluid Mech.* **399**, 319–333.

Bingham, H. B., Fuhrman, D. R., Jamois, E. & Kimmoun, O. 2004 Nonlinear wave interaction with bottom-mounted structures by a high-order Boussinesq method. In *Proc. 19th Intl Workshop Water Waves and Floating Bodies, Cortona, Italy*.

Dingemans, M. W. 1997 Water Wave Propagation over Uneven Bottoms. Part 1 – Linear Wave Propagation. World Scientific.

Fuhrman, D. R. & Bingham, H. B. 2004 Numerical solutions of fully non-linear and highly dispersive Boussinesq equations in two horizontal dimensions. *Intl J. Numer. Meth. Fluids* **44**, 231–255.

Hogan, S. J., Gruman, I. & Stiassnie, M. 1988 On the changes in phase speed of one train of water waves in the presence of another. *J. Fluid Mech.* **192**, 97–114.

Jiang, L., Perlin, M. & Schultz, W. W. 1998 Period tripling and energy dissipation of breaking standing waves. *J. Fluid Mech.* **369**, 273–299.

Longuet-Higgins, M. S. & Drazen, D. A. 2002 On steep gravity waves meeting a vertical wall: a triple instability. *J. Fluid Mech.* **466**, 305–318.

Longuet-Higgins, M. S. & Phillips, O. M. 1962 Phase velocity effects in tertiary wave interactions. *J. Fluid Mech.* **12**, 333–336.

Madsen, P. A., Bingham, H. B. & Liu, H. 2002 A new Boussinesq method for fully nonlinear waves from shallow to deep water. *J. Fluid Mech.* **462**, 1–30.

Mavrakos, S. A., Chatjigeorgiou, I. K., Grigoropoulos, G. & Maron, A. 2004 Scale experiments for the measurement of motions and wave run-up on a TLP model, subjected to monochromatic waves. In *Proc. 14th Intl Offshore and Polar Engng Conf., Toulon, France*, Vol. 1, pp. 382–389.

Molin, B. 1994 Second-order hydrodynamics applied to moored structures. A state-of-the-art survey. *Ship Technol. Res. (Schiffstechnik)* **41/2**.

Molin, B. 2001 Numerical and physical wavetanks: making them fit. *Ship Technol. Res. (Schiffstechnik)* **48/1**.

Molin, B. 2004 Interactions vagues–vagues et interactions vagues–structure. In *Actes de la Cinquième Rencontre Hydrodynamique Marine*. Casablanca (in French).

Molin, B., Remy, F. & Kimmoun, O. 2004 Experimental study of the non-linear wave interaction with a vertical plate. In *Proc. 14th Intl Offshore and Polar Engng Conf., Toulon, France*, Vol. 3, pp. 380–387.

Molin, B., Remy, F., Kimmoun, O. & Ferrant, P. 2003 Third-order interactions and wave run-up. In *Proc. 18th Intl Workshop Water Waves and Floating Bodies, Le Croisic, France*.

Swan, C., Taylor, P. H. & van Langen, H. 1997 Observations of wave–structure interaction for a multi-legged concrete platform. *Appl. Ocean Res.* **19**, 309–327.

Tanaka, M. 2002 On the phase velocity effect of nonlinear interactions between surface gravity waves. *Phys. Fluids* **14**, 2109–2112.